Ocean Color Hyperspectral Remote Sensing with High Resolution and Low Latency – the HYPSO-1 CubeSat Mission

Mariusz E. Grøtte, *Member, IEEE,* Roger Birkeland, *Member, IEEE,* Evelyn Honoré-Livermore, *Member, IEEE,* Sivert Bakken, *Member, IEEE,* Joseph L. Garrett, *Member, IEEE,* Elizabeth F. Prentice, *Member, IEEE,* Fred Sigernes, *Member, IEEE,* Milica Orlandić, *Member, IEEE,* J. Tommy Gravdahl, *Senior Member, IEEE,* Tor A. Johansen, *Senior Member, IEEE*

***Abstract*—Sporadic ocean color events with characteristic spectra, in particular algal blooms, call for quick delivery of high-resolution remote sensing data for further analysis. Motivated by this, we present the mission design of HYPSO-1, a 6U CubeSat at 500 km orbit altitude hosting a custom-built pushbroom hyperspectral imager with wavelengths between $387-801$ nm at bandpass of 3.33 nm and swath width of 70 km. The expected Signal-to-Noise Ratio is characterized for typical open ocean water-leaving radiance and can be flexibly increased by pixel binning. With the goal to enable better than 100 m spatial resolution, it is shown by geometric principles that the satellite may execute a slew maneuver to increase the number of overlapping pixels during a scan. Since generated high-dimensional hyperspectral data products need to be transmitted over limited space-ground communications, we have designed a modular FPGA-based onboard image processing architecture that aims to significantly reduce the data size without losing important spatial-spectral information. We justify the concept with a simulated scenario where HYPSO-1 first collects hyperspectral images of a 40 km by 40 km coastal area in Norway, and aims to immediately transfer these to nearby ground stations. With CCSDS123 lossless compression, it takes about one orbit revolution to obtain the complete data product when considering the overhead in satellite bus communications, and less than 10 min without the overhead. It is shown that even better latency can be achieved with advanced onboard processing algorithms.**

***Index Terms*—HYPSO-1, hyperspectral imaging, space optics, onboard processing, ocean color.**

Manuscript received September 17, 2020. This work was supported by the Research Council of Norway, Statoil?, DNV GL and Sintef through the Centers of Excellence funding scheme, Grant 223254 - Center for Autonomous Marine Operations and Systems (AMOS) and the Research Council of Norway through the IKTPLUSS programme grant 270959 (MASSIVE). This work is also supported by the Norwegian Space Centre contract SAT.01.17.7 and European Research Council on Informatics and Mathematics (ERCIM) postdoctoral fellowship. *Corresponding author: Mariusz E. Grøtte*

M. E. Grøtte, S. Bakken, J. L. Garrett, E. F. Prentice, F. Sigernes, J. T. Gravdahl, T. A. Johansen are with the Center for Autonomous Marine Operations and Systems (AMOS), Department of Engineering Cybernetics, Norwegian University of Science and Technology, Trondheim 7034, Norway (e-mail: mariusz.eivind.grotte@ntnu.no; sivert.bakken@ntnu.no; joseph.garrett@ntnu.no; elizabeth.prentice@ntnu.no; jan.tommy.gravdahl@ntnu.no; tor.arne.johansen@ntnu.no).

R. Birkeland, E. Honoré-Livermore and M. Orlandić are with Department of Electronic Systems, Norwegian University of Science and Technology, Trondheim 7491, Norway (e-mail: roger.birkeland@ntnu.no; evelyn.livermore@ntnu.no; milica.orlandic@ntnu.no).

F. Sigernes is also with the University Center in Svalbard, Longyearbyen 9171, Norway (e-mail: fred.sigernes@unis.no).

I. Introduction

HYPERSPECTRAL and multispectral remote sensing are typically used in the context of monitoring colorful processes with large spatio-temporal extents. A commonly observed phenomena of these is chlorophyll, a primary light-absorbing substance involved in phytoplankton photosynthesis which may have clear signatures at the water surface [1]. Blooms of phytoplankton have variable coloration and are often categorized as "red tides", "green tides" or "brown tides" with wavelengths between $400-700$ nm [1], [2], [3], [4], [5], [6]. They sporadically appear worldwide with varying biomass concentrations, may last from a few minutes to several days and cover regions from tens to hundreds of square kilometers [7]. Sometimes malignant, often identified as Harmful Algal Blooms (HABs) or cyanobacteria, such blooms may cause sudden damage to the marine environment, ecosystems and sustainable food sources [8]. According to [2], numerous plankton and algae types can be distinguished or inferred by their photosynthetic pigments and fluorescence, and hyperspectral data with capability of high spectral resolution may reveal the subtle spectral inflections imparted by specific pigment complements. However, determining the harmfulness of algae is not easily done from optical remote sensing alone, and is attributed to in-situ measurements in the upper water-column [2], [9]. Further challenges include atmospheric absorption and scattering of light [10], and the fact that the majority of biomatter typically reside at $10-15$ m below the water surface [2], such that these heterogeneous and potentially dark targets often demand a combination of larger space-based optics with high Signal-to-Noise ratio (SNR), rigorous atmospheric correction schemes and accompanied real-time in-situ measurements [11], [12].

Traditional Earth Observation (EO) satellites with large optical systems, several operated by National Aeronautics and Astronautics Administration (NASA) and European Space Agency (ESA), are designed to cover the Earth on a global scale and provide excellent ocean color data with medium to high spatial resolution [13], [14], but they normally offer low spectral resolution and revisit times of several days [15]. For example, using data products from Sentinel-3's Ocean Color and Land Instrument (OLCI) for detecting cyanobac-

terial blooms based on pigments such as phycocyanin and chlorophyll-a can be inaccurate using traditional ground-based analysis algorithms, unless employing newer algorithms that utilize band ratios from an alternate set of selected spectral bands [16]. Providing greater flexibility in namely choosing more than a hundred spectral bands instead of dozens [17], hyperspectral remote sensing missions show great promise in ocean color remote sensing, e.g. [18], [19], [20], [21], [22], [23], [24], [25], [26]. Yet, many of these stand-alone systems still lack the operational flexibility and revisit times to efficiently monitor dynamic areas on-demand [27]. Moreover, accurate but time-consuming and rigorous data processing methods are usually performed on ground together with synergistic analysis of in-situ measurements.

A small-satellite, often categorized as nano- or micro-satellite, normally has a short lifetime compared to traditional large satellites but can frequently be substituted with updated technology and has lower development and production costs [28]. Given recent advances in sensor technology, miniaturization and availability of commercial-off-the-shelf (COTS) products, custom-built hyperspectral imagers can now also be suited for use in nano-satellites [29], [30], [31], [32]. Instead of mapping on the global scale, single-purpose hyperspectral imaging small-satellites may focus on observing smaller dedicated areas more frequently to characterize temporal variation in both the spatial and spectral domains, also allowing a smaller camera system with relatively narrow Field-of-View (FoV). Choosing target areas on the sub-mesoscale or mesoscale, this has the potential enabling small-satellites to support a network of in-situ assets that may observe or sample with more detail in the spatial and spectral domains, e.g. Unmanned Aerial Vehicles (UAVs), Unmanned Surface Vehicles (USVs), Autonomous Underwater Vehicles (AUVs), and buoys [8]. To make such a multi-agent network function efficiently in real-time and reducing the operational costs, the remote sensing data must be quickly downloaded to keep validity in the highly time-varying information.

It is well-known that hyperspectral imagers generate large amounts of data that consequently take long time to transfer to ground due to limitations in bandwidth, coverage to ground stations and onboard computational resources [33], [27]. Reduction in data size onboard is crucial for satisfying real-time requirements but can also be difficult due to the limited power available per orbit for a small-satellite. Nevertheless, onboard processing has advanced significantly for remote sensing applications [34], in particular Field-Programmable Gate Arrays (FPGAs) that are reconfigurable and have high computational speed and low power consumption [35], [36]. Enabling algorithm parallelism, a modular FPGA-based image processing architecture allows for custom algorithms or image processing pipelines. Beyond standard losslessly compressed data, tailored end data products may contain only extracted spatial-spectral information generated from dimensionality reduction, target detection or classification [37], [38]. The significantly reduced data can therefore grant shorter waiting time between image acquisition to complete data download and be used for immediate utilization in real-time applications, e.g. for in-situ measurements or supporting an algal bloom warning systems [6], [39], [40].

With the goal to support environmental monitoring and the ocean color community by providing tailored hyperspectral data products with low latency, we present the mission design for the upcoming HYPer-spectral Smallsat for ocean Observation (HYPSO-1) developed at the Norwegian University of Science and Technology (NTNU). This paper is organized as follows. Section II describes the ocean color remote sensing needs that motivate the choice of imager, key remote sensing capabilities, and the HYPSO-1 Concept of Operations (CONOPS). Section III presents the design and performance of the custom pushbroom hyperspectral imager payload. Section IV describes our remote sensing approach supported by expected results from simulations involving a slew maneuver technique to enhance the spatial resolution in the image. In Section V, we present HYPSO-1, a 6U CubeSat, with its subsystems and power budget for nominal imaging, processing and downlink operations. In Section VI, we describe the chosen FPGA-based onboard image processing pipelines that shall deliver custom data products, provide a survey of potential onboard implementations of more advanced algorithms, and justify the HYPSO-1 mission feasibility with corresponding data latency for chosen imaging modes and the user-attuned data products. Finally, conclusions are provided in Section VII.

II. Mission Design

A. Objectives

The mission objectives of the HYPSO-1 are to monitor the spatio-temporal extent of ocean color events in the visual and near-infrared (VIS-NIR) wavelengths between $400-800$ nm; and to infer phytoplankton functional groups. Key user needs in the ocean color remote sensing are:

1) Images should have spatial resolution better than $30-100$ m per pixel [15], [41];
2) Raw hyperspectral data should have spectral resolution of about 5 nm for VIS-NIR wavelengths [15], [41];
3) The imager's SNR at Top of Atmosphere (ToA) should be greater than 400 in visual wavelengths for open ocean water [42], and atmospherically corrected SNR of water-leaving signals should be between $40-100$ [43];
4) Data latency should be less than 1 hr [44];
5) Revisit times to dedicated areas of interest should be $3-72$ hrs [44], [45].

Since HYPSO-1 is a single small-satellite, but the first in a prospective constellation, we focus on working towards the recommendations 1), 2), 3) and 4).

B. Image Acquisition Basics

Whereas several types of spectrometers can be integrated on aerial or space platforms [46], the passive pushbroom imager design is an attractive choice with good SNR [47], [48], [49]. Use of COTS components have also made this type of design more affordable, accessible and flexible [29], [30].

With the scan direction oriented towards the velocity direction, a pushbroom imager sequentially scans several lines,

N_x, each having instantaneous pixels, N_y and N_λ, forming a hyperspectral datacube shown in Fig. 1. N_y is the number of spatial pixels perpendicular to the scan direction and N_λ is the number of pixels along the spectral dimension. The horizontal and vertical components of the FoV are ϵ_w and ϵ_h respectively. The time elapsed between two consecutive lines, or frames, is expressed by the integration time $\Delta t = 1/FPS = \tau + \delta t$ where FPS is the frame rate, τ is the camera exposure time and δt is the read-out time.

High spectral resolution is required for discrimination of fine spectral features in the water-leaving signals, and high spatial resolution is desired to reduce the effects of spectral mixing or blur in the image pixels. Mounted on a satellite moving at high orbital speed, the drawback is strictly speaking a low spatial resolution along the scan direction. A work-around is to overlap more frames by tilting the imager backwards as it translates forward, similar to the method described in [50]. This results in an increased number partially overlapping pixels which can be utilized to enhance SNR or spatial resolution as trade-offs using image restoration techniques such as deconvolution or super-resolution [51]. For clarity, the Euclidean distance on ground between center pixels of two consecutive frames is taken to be the Sequential Ground Sampling Distance (SGSD) not to be confused with the commonly defined Ground Sampling Distance (GSD) between adjacent pixels in an instantaneous frame.

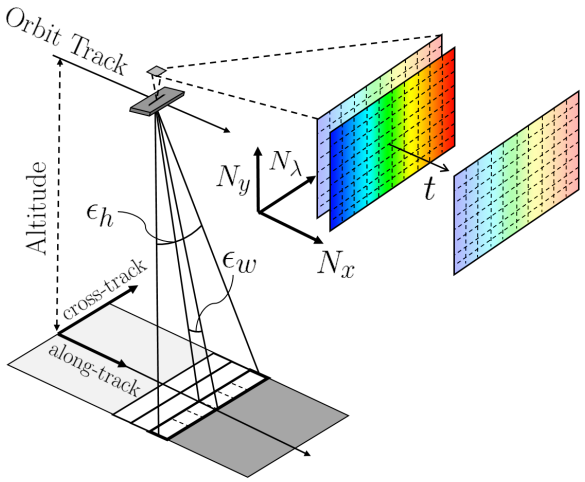

Fig. 1. Illustration of a pushbroom hyperspectral imager collecting N_x frames with N_λ and N_y pixels.

C. Concept of Operations

The overall mission utility and performance in HYPSO-1 is mainly engineered based on trade-offs in spatial resolution, spectral resolution, SNR, data size and latency, coverage to ground stations and likely locations for observations. HYPSO-1 will be launched to a $500\,\mathrm{km}$ altitude Sun-Synchronous Orbit (SSO) with Local Time of Descending Node (LTDN) at 10:00 AM, which grants early-day access to observe the Norwegian coastline during Spring and Summer seasons while avoiding detrimental sun-glint effects [52]. The HYPSO-1 mission concept of operations (CONOPS), illustrated in Fig. 2, enables five main capabilities:

1) After receiving telecommands and updates (e.g. camera settings) that are uploaded from a nearby ground station, HYPSO-1 is scheduled to orient its hyperspectral imager to start scanning a pre-defined area size;
2) HYPSO-1 executes a single-axis slew maneuver so that the imager's footprint slowly rotates backwards with respect to the scan direction. At a high camera frame rate, the goal is to enable a SGSD better than $100\,\mathrm{m/pixel}$.
3) After imaging, the hyperspectral images are processed onboard immediately to reduce their data size and speeding up the download on ground;
4) For quick downlink after observing coastal regions in Norway, the selected ground station network includes S-band ground stations at NTNU Trondheim, KSAT Svalbard, Norway, and KSAT Puertollano, Spain;
5) In addition, the Mission Control Center at NTNU operates several supporting robotic assets, such as UAVs, ASVs and AUVs, that may collect in-situ data if within range of the observed area.

D. System Capabilities

1) Imaging Modes: The hyperspectral imager has three main imaging configurations:

- High-resolution mode: enables high image resolution with narrow-FoV and high frame rate settings;
- Wide FoV mode: enables a wider swath but at coarser spatial resolution;
- Diagnostics mode: gives raw data with full sensor resolution to be mainly used for in-orbit calibration and characterization.

2) Attitude Determination & Control System: To obtain a spatial resolution better than $100\,\mathrm{m}$ requires a precise attitude determination and control system (ADCS) [31]. Throughout image acquisition for a satellite that is pointing or maneuvering, the attitude sensor noise and actuator inaccuracies (e.g. reaction wheel jittering) will contribute to a non-uniform distribution of images across the observed scene. The attitude errors are categorized as attitude control and knowledge accuracies, bearing in mind that performance of latter affects the former. For consistent image registration, or simply knowing the location of each pixel to the accuracy of $100\,\mathrm{m}$ on ground, e.g. geo-referencing, then good performance is needed for attitude knowledge accuracy, orbit position accuracy, and time synchronization between the captured images and attitude data.

3) On-board Image Processing: The image processing architecture should be modular by design with the goal to ease satellite operations and provide tailored data to end users at a low data latency. To make such data products useful, the high-level goals are to:

- Reduce hyperspectral data size onboard to improve data latency, by lossless compression at minimum;
- Extract the spatial and spectral information in water-leaving signals, by e.g. dimensionality reduction, target detection or classification;
- Register images and utilize the obtained SGSD to achieve better than $100\,\mathrm{m/pixel}$ image resolution using image restoration methods, e.g. deconvolution or super-resolution;

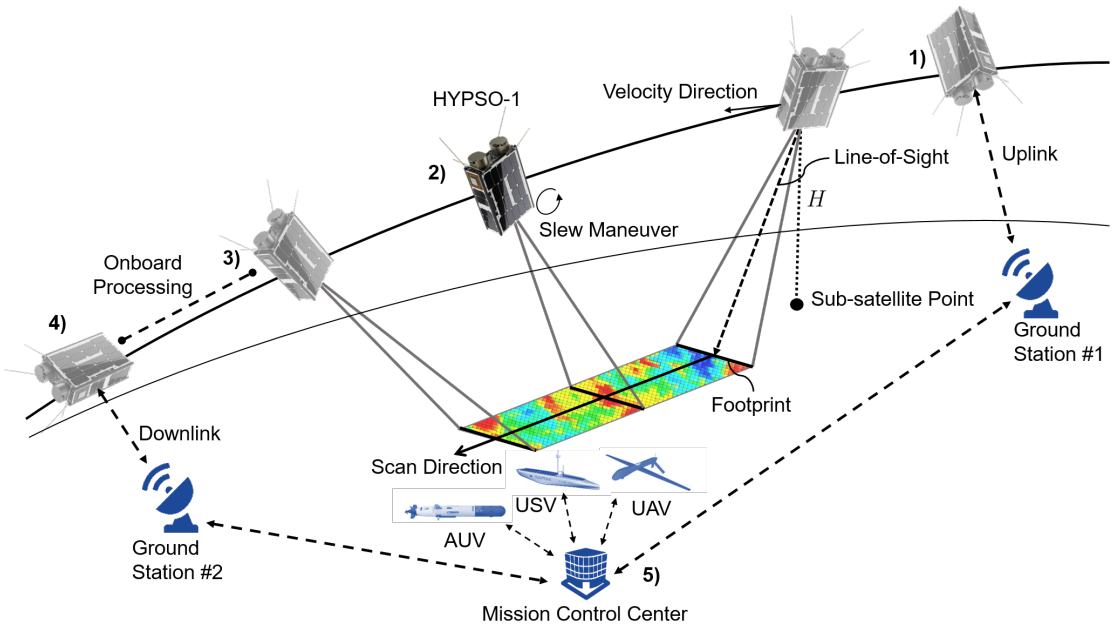

Fig. 2. CONOPS where 1) HYPSO-1 receives uplinked configurations from a nearby ground station; 2) acquires hyperspectral images for a short duration under a slew maneuver; 3) processes the images onboard immediately; 4) downlinks the data to nearby ground stations; and 5) in-situ assets in the vicinity may be deployed for closer investigation at the observed scene.

- Transform pixel indices to geodetic latitude and longitude by geo-referencing such that these coordinates can be used to guide in-situ agents towards interesting locations;

In the commissioning phase, the hyperspectral data products shall be analyzed in synergy with other available remote sensing data and in-situ measurements. Modeling and simulation tools shall also provide supporting information on atmospheric correction and the radiometric, spectral and spatial properties of a simulated ocean color event [53], [54].

III. Hyperspectral Imager Design

A. Optics

An optical diagram of the instrument with its cross-section parallel to the refraction axis is shown in Fig. 3, [48]. The labelled components are: (i) front lens with aperture diameter D_0 and focal length F_0; (ii) entrance slit with width w_{slit} and height h_{slit}; (iii) collimator lens with aperture diameter D_1 and focal length F_1; (iv) grating receiving incoming light at angle $\alpha = 0°$ and diffracts the light at angle β measured from the grating normal; (v) detector lens with aperture diameter D_2 and focal length F_2; and finally (vi) is the image sensor. The FoV components along and perpendicular to the scan-direction are expressed as

$$\tan\left(\frac{\epsilon_w}{2}\right) = \frac{w_{\text{slit}}}{2F_0}, \tag{1a}$$

$$\tan\left(\frac{\epsilon_h}{2}\right) = \frac{h_{\text{slit}}}{2F_0}. \tag{1b}$$

Assuming no loss of transmitting light from front lens to image sensor, the geometric etendue is expressed as

$$G = \pi \frac{D_0^2}{4F_0^2} \cos(\beta) w_d h_d, \tag{2}$$

where the magnification of the entrance slit onto the image sensor are

$$h_d = h_{\text{slit}} \frac{F_2}{F_1}, \tag{3a}$$

$$w_d = \frac{w_{\text{slit}} F_2}{\cos(\beta) F_1}, \tag{3b}$$

and β is the diffraction angle for the center wavelength [55]. As shown in Fig. 4, the amount of illuminated pixels of projected slit width and height onto the image sensor are

$$N_h = \frac{h_d}{\Delta p_y}, \tag{4a}$$

$$N_w = \frac{w_d}{\Delta p_\lambda}, \tag{4b}$$

where Δp_λ and Δp_y are the pixel width and height, respectively.

The theoretical bandpass for the optical system, or the recorded Full Width at Half Maximum (FWHM) of a monochromatic spectral line, indicates how well adjacent spectral lines are resolved. Assuming no degradation due to aberrations and diffraction, the spectral bandpass may be approximated as

$$\Delta\lambda \approx \frac{g w_{\text{slit}}}{\kappa F_1}, \tag{5}$$

where g is the groove spacing of the grating and κ is the spectral order [55].

B. Payload Flight Model

HYPSO-1's hyperspectral imager payload is mainly built with COTS products from Thorlabs and Edmund Optics and a

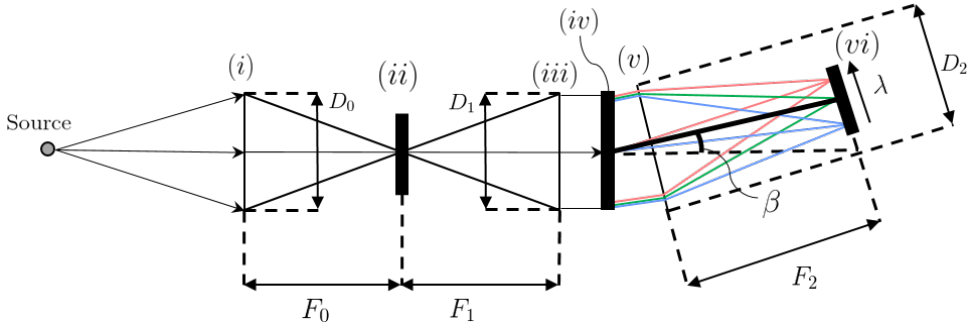

Fig. 3. Optical diagram of the cross-section of the pushbroom hyperspectral imager. The light is focused into a slit, collimated into a grating which then diffracts the light into an image sensor plane.

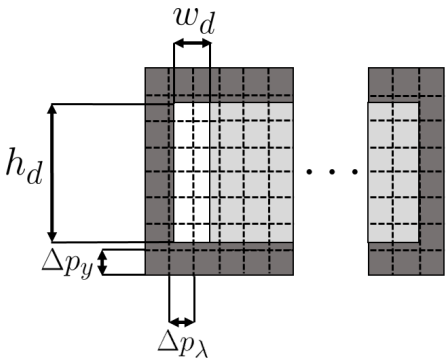

Fig. 4. Illustration of the projected slit onto the image sensor plane with h_d and w_d dimensions with the white region corresponding to one spectral band. The camera's mechanical layout may block some of the light as indicated by the dark gray regions. In practice, weaker signals can be expected in the pixels at the edges compared to central pixels since they are partially illuminated.

few custom machined parts [29], shown in Fig. 5. The imager is designed to provide a spectral range of at least $400-800$ nm and theoretical spectral bandpass of 3.33 nm. The focal length for each lens should be equal to maximize the light throughput, but to avoid detrimental stray light effects the F-numbers are set to $F_0/\# = F_1/\# = 2.8$ and $F_2/\# = 2$. The instrument's key specifications are given in Table I.

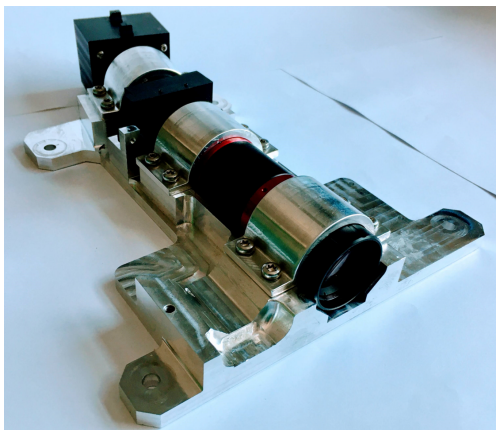

Fig. 5. Hyperspectral imager payload assembled for CubeSat integration

A SONY IMX249 image sensor is mounted in an industrial camera head from The Imaging Development Systems Europe GmbH. It has 1936×1216 pixels with reported well depth of about 33022 e^- per pixel equivalent to maximum SNR of approximately 181.6. The maximum FPS is limited by the data throughput, number of binning operations, subsampling and Area of Interest (AoI), where latter is the selected number of pixels in a custom image sensor window.

TABLE I
HYPERSPECTRAL IMAGER SPECIFICATIONS

Parameter	Value
Dimensions	200 mm × 65 mm × 65 mm
Weight	1.6 kg
FoV $\epsilon_w \times \epsilon_h$	$0.0564° \times 7.8826°$
$F_0 = F_1 = F_2$	50 mm
$F_0/\# = F_1/\#$	2.8
$F_2/\#$	2
$D_0 = D_1$	17.9 mm
D_2	25 mm
Slit width w_{slit}	50 μm
Slit height h_{slit}	7 mm
Optical efficiency $\eta_0 = \eta_1 = \eta_2$	0.8
Grating efficiency η_G @500 nm	0.73
Spectral order κ	1
Groove spacing g	3333.33 nm
Diffraction angle β	10.37°
Pixel size $\Delta p_\lambda = \Delta p_y$	5.86 μm
Usable sensor resolution	1936×1194 pixels
Quantum efficiency η_Q @500 nm	0.77
Full spectral range	$220 - 967$ nm
Spectral bands at full resolution	at least 215
Theoretical bandpass $\Delta\lambda$	3.33 nm
Dark current i_{dark}	0.95 e^-/s
Read-out noise $C_{\text{read-out}}$	6.93 e^-
Quantization noise C_{quant}	2.33 e^-
Max. SNR per pixel (unbinned)	181.6 (45.2 dB)
ADC bit-depth b	12 bits

C. Characterizing Signal-to-Noise Ratio

SNR is a measure of the instrument's sensitivity to light and ability to resolve spectral signatures that are subject to correlated signal noise and uncorrelated image sensor noise. A high SNR is needed for better radiometric accuracy and discriminating the dimmer optical constituents in water scenes for in-orbit calibration, atmospheric correction and algorithms such as target detection or classification. However, increasing SNR, either by optical design or image processing, is a trade-off with coarser spatial resolution or spectral resolution.

The incoming light reaching the imager's front lens can be represented by the total radiance at Top-of-Atmosphere (ToA), comprised of several components that are functions of wavelength and viewing direction [56], [57],

$$L_{\text{tot}}^{\text{ToA}} = L_{\text{atm}}^{\text{ToA}} + t_{\text{dir}} L_{\text{sg}} + t_{\text{diff}} L_{\text{wc}} + t_{\text{diff}} L_{\text{water}} \tag{6}$$

where $L_{\text{atm}}^{\text{ToA}}(\lambda)$ is the combined radiance of Rayleigh, aerosol and Rayleigh-aerosol interaction scattering including sky background reflection and scattering, and $L_{\text{sg}}(\lambda)$, $L_{\text{wc}}(\lambda)$ and $L_{\text{water}}(\lambda)$ are the surface-based specular reflection of sun glint radiance, sun and sky radiance reflected by whitecaps and foam, and the water-leaving radiance, respectively. The terms $t_{\text{dir}}(\lambda, \gamma; H)$ and $t_{\text{diff}}(\lambda, \gamma; H)$ are the direct and diffuse transmittances along the optical path governed by wavelength, viewing angle γ and altitude above the surface H.

Generalizing for a reference signal component to be detected at ToA, $L_{\text{ref}}^{\text{ToA}}(\lambda)$, this can be a chosen term of interest from (6), i.e. the total ToA radiance $L_{\text{ref}}^{\text{ToA}}(\lambda) = L_{\text{tot}}^{\text{ToA}}(\lambda)$ or a component thereof, i.e. the water-leaving radiance $L_{\text{ref}}^{\text{ToA}}(\lambda) = L_{\text{water}}^{\text{ToA}}(\lambda)$. The corresponding photon flux per spectral bandpass reaching the image sensor is

$$\dot{\Phi}_{\text{ref}}^{\text{ToA}} = L_{\text{ref}}^{\text{ToA}} \eta_0 \eta_1 \eta_G \eta_2 G \lambda \frac{\Delta\lambda}{h_{\text{planck}} c}, \tag{7}$$

where $L_{\text{ref}}^{\text{ToA}}(\lambda)$ is the reference radiance, η_0, η_1, η_2 are the optical efficiencies of the front, collimator and detector lenses respectively, $\eta_G(\lambda)$ is the grating efficiency, c is the speed of light, and $h_{\text{planck}} = 6.62607015 \times 10^{-34}$ Js is Planck's constant. The count of photon-electrons per pixel is

$$C_{\text{ref}} = \frac{\eta_{\text{Q}} \dot{\Phi}_{\text{ref}}^{\text{ToA}} \tau}{N_w N_h}, \tag{8}$$

where $\eta_{\text{Q}}(\lambda)$ is the quantum efficiency of the image sensor. Assuming that $C_{\text{ref}}(\lambda)$ has a Poisson probability distribution [58], [59], the SNR for a signal at ToA can be expressed as

$$SNR_{\text{ref},[1,1]} = \frac{C_{\text{ref}}}{\sqrt{C_{\text{ref}} + C_{\text{dark}} + C_{\text{read-out}}^2 + C_{\text{quant}}^2}}, \tag{9}$$

where $C_{\text{dark}} = i_{\text{dark}} \Delta t$ has a Poisson probability distribution, while $C_{\text{read-out}}$ and C_{quant} have Gaussian probability distribution with zero mean [58], [59]. The average shot noise registered due to the dark current i_{dark} is $i_{\text{dark}} \Delta t$, $C_{\text{read-out}}$ is the standard deviation of electrons in the sensor read-out circuits, and $C_{\text{quant}} = C_{\text{max}}/(2^b \sqrt{12})$ is the standard deviation of quantization noise where C_{max} is the well depth and b is the Analog-to-Digital Converter (ADC) bit depth. SNR of less than 1 results in non-resolvable features fully obscured by noise. On the other hand, a high SNR per pixel is limited by the image sensor's saturation capacity or well depth.

1) Binning: With the ability to bin pixels on the image sensor, photon-electrons can be gathered from adjacent pixels to create a merged pixel with higher SNR as the signal synthetically increases proportionally with the square root of number of binning operations. To increase the SNR without losing spectral resolution, one may fully bin the number of pixels covered by the spectral bandpass. Therefore, $B_\lambda = \lceil N_w \rceil$ pixels can be binned where B_λ is the number of binning operations in the spectral direction and $\lceil \cdot \rceil$ indicates rounding up to nearest integer. This results in the effective SNR to be $SNR_{\text{ref},[\lceil N_w \rceil,1]} \approx \sqrt{N_w} SNR_{\text{ref},[1,1]}$. Similarly, B_y binning operations in the instantaneous spatial direction along h_d, also results in higher SNR but at the cost of spatial resolution.

2) SNR of total ToA radiance: Atmospheric effects significantly augment the light in the imager's optical path, such that the water-leaving radiance at the surface, L_{water}, may only constitute a mere 10% of the total ToA radiance $L_{\text{tot}}^{\text{ToA}}$ [60], [61]. The total radiance at ToA for open ocean water is typically between $0.005 - 0.06\ \text{Wm}^{-2}\text{sr}^{-1}\text{nm}^{-1}$ in the spectral range of $400 - 800$ nm with strongest signals in the blue-green wavelengths and decreasing towards the red part of the spectrum [62]. Assuming $L_{\text{tot}}^{\text{ToA}} = 0.042\ \text{Wm}^{-2}\text{sr}^{-1}\text{nm}^{-1}$ at 500 nm based on [62], and setting $\tau = 51.6$ ms, this would amount to $SNR_{\text{total},[1,1]} \approx 133$ and $SNR_{\text{total},[9,1]} \approx 392$ if binning of $B_\lambda = 9$ is used. For $B_\lambda = 18$, then $SNR_{\text{total},[18,1]} \approx 554$ at the cost of spectral resolution being worse than $\Delta\lambda = 6.67$ nm. Noteworthy, a radiance of $L_{\text{tot}}^{\text{ToA}} = 0.0725\ \text{Wm}^{-2}\text{sr}^{-1}\text{nm}^{-1}$ at 525 nm would give $SNR_{\text{total},[1,1]} \approx 182$ which is above the saturation capacity at SNR of 181.6. If pixels that are not binned saturate at wavelengths of interest, then one could decrease the sensor's exposure time τ.

3) SNR of open ocean water: To estimate the imager's SNR_{water}, we have used publicly available and calibrated water-leaving radiance measurements from the Marine Optical BuoY (MOBY) deployment number 267 off the coast of Hawaii [63], time-stamped at 21:11:38 GMT on 3 July 2019. The data on that particular day are typical for open ocean water which is considered to be a good example for a scene observed by HYPSO-1, even though the signals are weak towards the red part of the spectrum. Fig. 6 shows the MOBY water-leaving radiance measurements, $L_{\text{water}}(\lambda)$, and the simulated water-leaving radiance at ToA, $L_{\text{water}}^{\text{ToA}}(\lambda) = t_{\text{diff}}(\lambda, \gamma, H) L_{\text{water}}(\lambda)$. The MOBY measurements are fitted with a spline curve to match the theoretical bandpass of the hyperspectral imager in the wavelength range of $400{-}750$ nm. The water-leaving signal reaching ToA is assumed to be weakened by only the Rayleigh optical thickness part of the transmittance model, based on [64]. This assumption does not include other contributing atmospheric effects that partially govern $L_{\text{tot}}^{\text{ToA}}$, e.g. Rayleigh scattering, aerosol scattering, Rayleigh-aerosol interactions and sun reflection [60]. A more realistic atmosphere can be modeled for complete details.

Simulated using (7), (8) and (9), Fig. 7 shows the estimated SNR_{water} at ToA in the $400 - 750$ nm spectral range for the hyperspectral imager sensing the water-leaving radiance $L_{\text{ref}}^{\text{ToA}} = L_{\text{water}}^{\text{ToA}}$ with $\gamma = 0°$ and $\tau = 51.6$ ms. The target SNR at a chosen wavelength of 500 nm increases from $SNR_{\text{water},[1,1]} = 45.8$ to $SNR_{\text{water},[9,1]} = 134.8$ with $B_\lambda = 9$, to $SNR_{\text{water},[18,1]} = 190.6$ with $B_\lambda = 18$ and to $SNR_{\text{water},[26,1]} = 233.5$ with $B_\lambda = 26$. With no binning and at $B_\lambda = 9$ then $\Delta\lambda = 3.33$ nm while $B_\lambda = 18$ and $B_\lambda = 26$ result in $\Delta\lambda = 6.67$ nm and $\Delta\lambda = 10$ nm, respectively. The estimated performance at $B_\lambda = 9$ accommodates the recommended SNR of at least $40 - 100$ for water-leaving signals [43]. Moreover, the effective image SNR in a complete

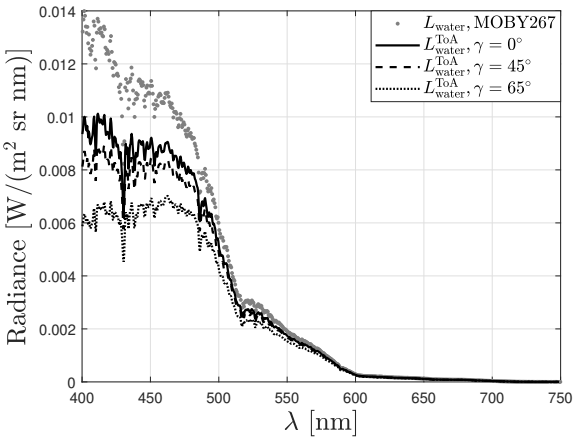

Fig. 6. Water-leaving radiance, L_{water}, measured by MOBY267 and estimated water-leaving radiance at ToA, $L^{\text{ToA}}_{\text{water}}$, for different viewing angles γ.

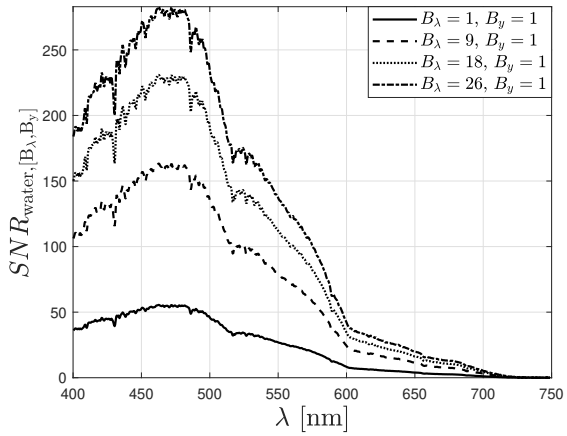

Fig. 7. SNR per pixel for the estimated $L^{\text{ToA}}_{\text{water}}$ component with exposure time $\tau = 51.6$ ms and a selected number of binning operations.

datacube can be further increased given that spatial pixels overlap over the same local scenes.

IV. Remote Sensing Approach

A. Attitude Definition

Shown in Fig. 8, the orthonormal vectors $\hat{\mathbf{x}}_b$, $\hat{\mathbf{y}}_b$ and $\hat{\mathbf{z}}_b$ define the body frame and are aligned with the satellite's principal axes of inertia. The hyperspectral imager is assumed to be mounted with its optical axis along $\hat{\mathbf{z}}_b$, the slit height h_{slit} aligned with $\hat{\mathbf{y}}_b$ and the slit width w_{slit} aligned with $\hat{\mathbf{x}}_b$. The satellite's orbit frame is defined by $\hat{\mathbf{x}}_o$ being aligned with the velocity vector, $\hat{\mathbf{y}}_o$ points towards the negative orbit normal vector, and $\hat{\mathbf{z}}_o$ is the nadir unit vector aligned with the opposite inertial position vector as seen in the Earth-Centered-Inertial (ECI) frame. The rotation of the body relative to the orbit frame are represented by Euler angles ϕ, θ and ψ which are the roll, pitch and yaw angles with $\phi = \theta = \psi = 0°$ at nadir. Attitude errors from references ϕ_{ref}, θ_{ref}, ψ_{ref} are $\delta\phi = \phi_{\text{ref}} - \phi$, $\delta\theta = \theta_{\text{ref}} - \theta$, $\delta\psi = \psi_{\text{ref}} - \psi$. For simplicity, it is assumed that the Earth is spherical such that the nadir vector $\hat{\mathbf{z}}_o$ coincides with the line that defines the local altitude H. Furthermore, ω_x, ω_y, and ω_z are the angular velocities of the satellite body frame relative to the orbit frame.

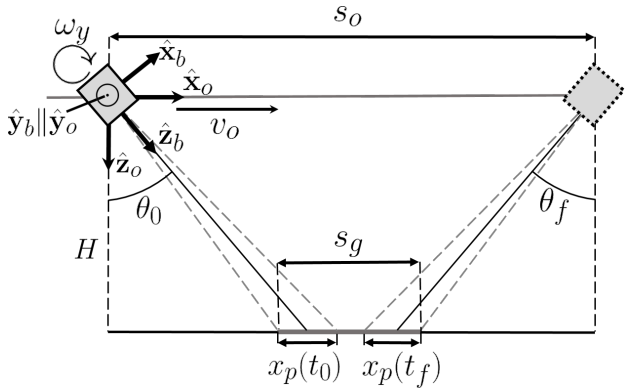

Fig. 8. Observation geometry at altitude H covering the orbital distance s_o while translating at speed v_o and slewing with angular velocity ω_y. The objective is to acquire images along the ground distance s_g from starting angle θ_0 to final angle θ_f. The starting and final instantaneous along-track footprints are $x_p(t_0)$ and $x_p(t_f)$. The axes $\hat{\mathbf{y}}_b$ and $\hat{\mathbf{y}}_o$ point out of the paper.

B. Instantaneous Resolution

Using (1a) and (1b), the instantaneous footprint of the hyperspectral imager, expressed in horizontal and vertical components, are

$$P_w = H \sec\phi \left(\tan\left(\theta + \frac{\epsilon_w}{2}\right) - \tan\left(\theta - \frac{\epsilon_w}{2}\right)\right), \quad (10a)$$

$$P_h = H \sec\theta \left(\tan\left(\phi + \frac{\epsilon_h}{2}\right) - \tan\left(\phi - \frac{\epsilon_h}{2}\right)\right), \quad (10b)$$

which are transformed to along-track and cross-track components of a central pixel as

$$x_p \triangleq \cos(\psi) P_w + \sin(\psi)\frac{P_h}{N_y}, \quad (11a)$$

$$y_p \triangleq \cos(\psi)\frac{P_h}{N_y} - \sin(\psi) P_w. \quad (11b)$$

In reality, ground-projected pixels near the edge of the swath are elongated compared to the central pixel. Along with effects from Earth curvature, these distortions are known as "bowtie effect" which can be corrected in post-processing [65], [66]. We note that the ground pixel size is taken to be relatively small, i.e. on a meter-scale, and pixel elongation and curvature can be ignored for a combination of high frame rate and narrow FoV.

C. Spatial Resolution

Now adding translational and rotational motion effects to the instantaneous footprint in (11a) and (11b) during exposure time τ, the along-track and cross-track spatial resolution in a pixel are

$$\Delta x = x_p + v_{p,x}\tau, \quad (12a)$$

$$\Delta y = y_p + v_{p,y}\tau, \quad (12b)$$

where $v_{p,x}$ and $v_{p,y}$ are the along-track and cross-track speeds of the pixels defined as

$$v_{p,x} \triangleq v_o + \dot{\theta}H - \dot{\psi}H\tan(\phi), \tag{13a}$$

$$v_{p,y} \triangleq -\dot{\phi}H + \dot{\psi}H\tan(\theta), \tag{13b}$$

where v_o is the satellite's orbital speed. Shown in Fig. 9, the

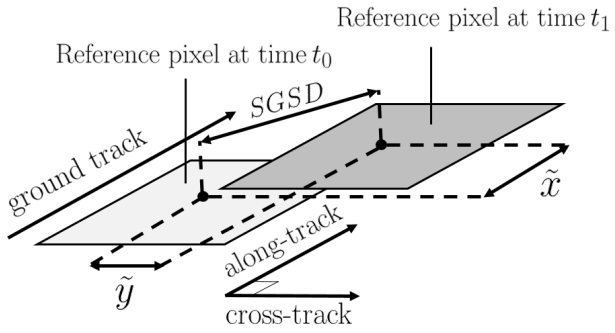

Fig. 9. A pixel moving by the distance SGSD from time t_0 to t_1.

SGSD may be defined as the distance a reference pixel has moved during integration time Δt, expressed in along-track and cross-track components as

$$\tilde{x} \triangleq v_{p,x}\Delta t, \tag{14a}$$

$$\tilde{y} \triangleq v_{p,y}\Delta t. \tag{14b}$$

The SGSD determines the amount of overlap of two sequential frames. Since x_p is significantly larger than y_p, and if the scan direction is aligned with the along-track direction at high orbital speed, then it is preferred to slew about the $\hat{\mathbf{y}}_o$ axis to enable better along-track spatial resolution. Noting from (13a) and (13b), the required angular velocity of the satellite ω_y may be obtained from the desired $\tilde{x}$ or vice versa.

D. Image Acquisition Strategy

Consider the ground length s_g to be uniformly scanned during time $\Delta T = t_f - t_0$ where the satellite rotates from starting to final pitch angles $\theta(t_0) = \theta_0$ and $\theta(t_f) = \theta_f$, as shown in Fig. 8. Assuming a local linear track for relatively short ΔT and small s_g, the final pitch angle can be set to $\theta_f = -\theta_0$ such that $x_p(t_0) = x_p(t_f)$. Furthermore, it is assumed that $\omega_x = \omega_z = 0^\circ/\text{s}$ and $\phi = \psi = 0^\circ$ such that $\omega_y = \dot{\theta}$ [67].

Setting the final pitch angle to $\theta_f = -\theta_0$, the covered orbit track distance can be calculated as

$$s_o = s_g + 2H\tan\left(\theta_0 - \frac{\epsilon_w}{2}\right), \tag{15}$$

where for a constant orbital speed v_o, the total time required for the slew maneuver to go from θ_0 to $-\theta_0$ is

$$\Delta T = \frac{s_o}{v_o}, \tag{16}$$

which gives the constant reference angular velocity

$$\omega_{\text{ref},y} = \dot{\theta}_{\text{ref}} = \frac{\Delta\theta}{\Delta T} = -\frac{2\theta_0}{\Delta T}. \tag{17}$$

For the case of a single-axis slew maneuver about the $\hat{\mathbf{y}}_o$ axis, Fig. 10 shows the required angular velocity $\omega_{\text{ref},y}$ at $H = 500$ km as a function of chosen $\theta_0 = -\theta_f$ for different s_g. Higher altitude or longer s_g demands slower rotation to obtain a constant SGSD.

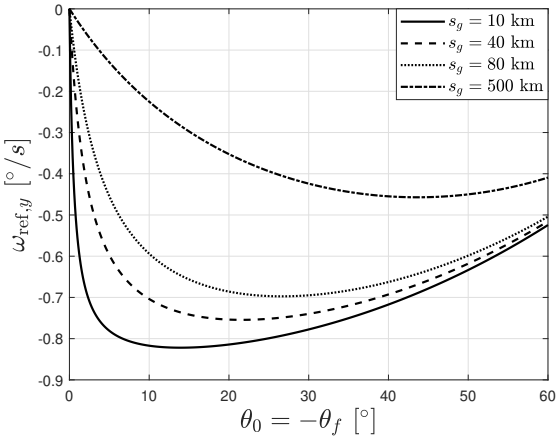

Fig. 10. Required angular vielocity $\omega_{\text{ref},y}$ vs. pitch angles $\theta_0 = -\theta_f$ for uniformly imaging different ground lengths s_g at $H = 500$ km.

E. Simulation Results

1) Resolution for Nadir-pointing: With the scan direction aligned to along-track, the instantaneous along-track and cross-track ground resolution at nadir are $x_p = 500$ m and $y_p = 58.6$ m respectively. It takes $\Delta T = 5.2$ s to scan the ground distance $s_g = 40.08$ km. Using the specifications in Table I and camera settings in Table II, the obtained spatial resolution becomes $\Delta x = 892.5$ m, $\Delta y = 58.6$ m with a swath width of $P_h = 40.08$ km. The along-track SGSD becomes $\tilde{x} = 422.9$ m, meaning that 3 frames partially overlap.

TABLE II
SIMULATION PARAMETERS

Parameter	Value
Frame rate FPS	18
Camera integration time Δt	55.6 ms
Camera exposure time τ	51.6 ms
Camera read-out time δt	4 ms
Target length s_g	40.08 km
Altitude H	500 km
Satellite speed v_o	7.61 km/s
Roll angle ϕ	0°
Yaw angle ψ	0°

2) Resolution for Slew Maneuver: Assuming $\omega_y = \omega_{\text{ref},y}$ where no attitude errors are present, and using the parameters in Tables I and II, Figs. 11 and 12 show how spatial resolution varies with slew maneuvers starting from θ_0 at $0^\circ, 10^\circ, 20^\circ$ and 30° and ending at $\theta_f = -\theta_0$. For these configurations, Table III shows the corresponding angular velocities required, observation time and along-track SGSD. Choosing $\theta_0 = 20^\circ$ and $s_g = 40.08$ km, the satellite would have to slew at angular velocity of $\omega_y = -0.754^\circ/\text{s}$ for 53.1 s to obtain a constant along-track SGSD of 57.6 m. The along-track spatial resolution varies between $\Delta x = 619.6$ m at $\theta = 20^\circ$ to a

minimum of $\Delta x = 553.4$ m at nadir, while the cross-track spatial resolution varies between $\Delta y = 62.4$ m at $\theta = 20°$ to a minimum of $\Delta y = 58.6$ m at nadir. With $\tilde{x} = 57.6$ m this means there will be at least 10 frames that partially overlap in the along-track direction. With this many overlapped spatial pixels of the same scene, the effective SNR in the final image may theoretically increase with a factor of up to $\sqrt{10}$ times, i.e. 83% more than for a nadir-pointing scan. However, in practice, the further increase in SNR can be lower due to trade-off with desired high spatial resolution when using image restoration techniques.

3) Attitude Errors: Precise attitude control accuracy is needed for directly obtaining the desired SGSD between two sequential frames at any time during image acquisition. Referring to the image resolution requirement of less than 100 m as discussed in Section II, and using (14a) and (13a), we have the requirement for angular velocity accuracy being

$$|\delta\dot{\theta}_c| < \frac{|x^* - \tilde{x}|}{H\Delta t} - \frac{v_o}{H} + \dot{\psi}\tan(\phi) - \dot{\theta}_{\text{ref}}, \tag{18}$$

where x^* is the desired upper limit of SGSD between two frames captured after each other. It can be assumed that the term $\dot{\psi}\tan(\phi) \approx 0$ for small ϕ and ψ. Using the parameters in Table II, and choosing angular velocity of $\dot{\theta}_{\text{ref}} = -0.754$ deg/s, along-track SGSD of $\tilde{x} = 57.6$ m and setting $x^* = 100$ m, the angular velocity errors must be less than 0.094 deg/s throughout image acquisition.

The attitude error problem can be relaxed to rather focus on obtaining sufficient attitude knowledge for the purpose of consistent image registration and geo-referencing. Assuming low uncertainty in orbit position and a precise on-board time-synchronization, then for pixel-to-pixel distance errors to remain within the bound of ±100 m, using (1a) and (11a), the attitude knowledge error requirement is

$$|\delta\theta_k| < \tan^{-1}\left(\frac{|x^*|}{H\sec(\phi)} + \tan(\theta_{\max})\right) - \theta_{\max}, \tag{19}$$

where $\theta_{\max}$ is the largest desired angle during image acquisition. Given a desired SGSD of $\tilde{x} = 57.6$ m at $\theta_{\max} = 20°$ and $\phi = 0°$, using (19) and assuming $\sec(\phi) \approx 1$, the required attitude knowledge accuracy must be better than 0.01°. Table III shows the required attitude knowledge accuracy for other slew maneuver configurations.

TABLE III
SLEW MANEUVER RESULTS FOR $s_g = 40.08$ km AND $FPS = 18$

Configuration	θ_0 [°]	ω_y [°/s]	ΔT [s]	$\tilde{x}$ [m]	$\lvert\delta\theta_k\rvert$ [°]
1	0	0	5.2	422.9	0.0088
2	10	-0.704	28.4	81.8	0.0111
3	20	-0.754	53.1	57.6	0.0102
4	30	-0.740	81.1	64.3	0.0086

V. HYPSO-1 SYSTEM

A. Satellite Bus

The hyperspectral imager was chosen to be adapted to the Multipurpose 6U Platform (M6P), a commercially available spacecraft bus provided by NanoAvionics, with mass

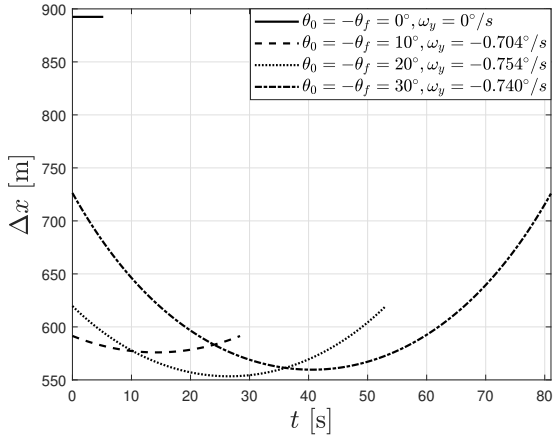

Fig. 11. Along-track spatial resolution for chosen configurations of pitch angles $\theta_0 = -\theta_f$ and angular velocities ω_y.

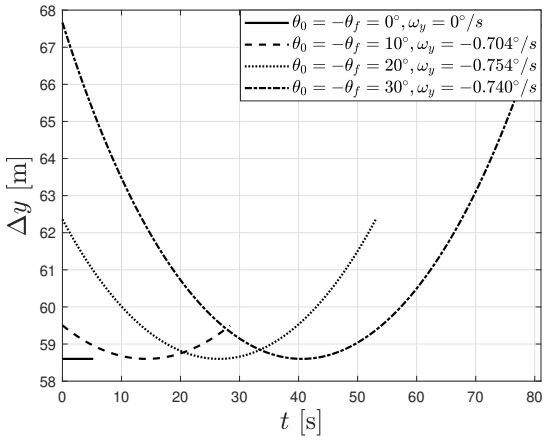

Fig. 12. Cross-track spatial resolution for chosen configurations of pitch angles $\theta_0 = -\theta_f$ and angular velocities ω_y.

of approximately 6.8 kg when fully integrated. Among the important subsystems in M6P are Flight Computer (FC) for onboard data handling and ADCS functions, SatLab Global Navigation Satellite System (GNSS) for orbit determination and time synchronization, Electrical Power System (EPS), Ultra-High-Frequency (UHF) radio for basic space-ground communications, and Payload Controller (PC) working as storage device and router between the payload and the satellite bus. For internal communications, the spacecraft uses the CubeSat Space Protocol (CSP) over a Controller Area Network (CAN), where each subsystem is a network node with dedicated CSP address. The M6P has 16 body-mounted triple junction Gallium Arsenide solar cells and six Lithium-Ion batteries with total energy capacity of 64.9 Wh.

B. Dedicated Subsystems

To fulfill the user needs and mission CONOPS described in Section II, HYPSO-1 is further equipped with:

- A Nano Star Tracker ST-1 [68] and Sensonor STIM 210 Inertial Measurment Unit (IMU) [69] used for precise

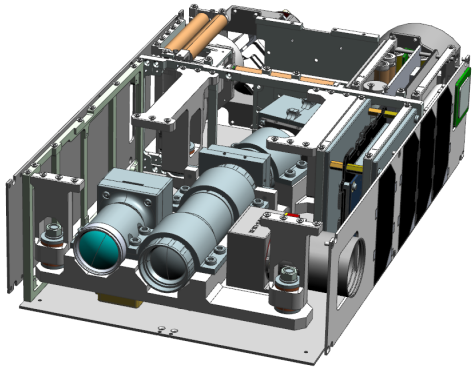

Fig. 13. Computer-Aided Drawing (CAD) model of HYPSO-1 with its top and front panels removed showing the hyperspectral imager in the center, RGB camera to its left and star-tracker to its right.

attitude estimation during imaging. To ensure sufficient settling time after initialization, the sensors are turned on for at least 5 min prior to imaging. When images will not be taken, then six sun sensors, three magnetometers and three gyroscopes are used instead which provide coarser attitude knowledge but consume less power;

- Four reaction wheels used for attitude control that provide up to 3.2 mNm torque each, where three are placed orthogonally along the body axes and the fourth is tilted at an angle of $54.7°$. Two magnetorquers are placed along each body axis for reaction wheel momentum dumping;
- An IDS UI-125x RGB camera with 6 mm $F/1.4$ Ci series fixed lens providing a footprint of 770 km $\times$ 540 km and spatial resolution of approximately 500 m. Its main purpose is to support and validate hyperspectral images in the spatial domain [70];
- A 2.4 GHz IQ Spacecom S-band Transceiver providing usable data rate of 1 Mbps for downlinking payload data;
- An Onboard Processing Unit (OPU) hosting a Zynq-7030 Xilinx PicoZed System-on-a-Chip (SoC) with flight heritage [34]. It consists of two core ARM processors and a Field Programmable Gate Array (FPGA) dedicated for onboard image processing. The OPU allows for in-orbit updates of both software and FPGA hardware reconfigurations for uploaded algorithms. Larger data sizes can be buffered from the OPU to the PC over CAN before downlinking over S-band radio, or smaller amounts of data can be downloaded directly from the OPU. Buffering data to the PC enables full utilization of the S-band data rate, and removes the need for keeping the OPU turned on for longer than necessary. Power and data-line distribution to the hyperspectral and RGB cameras are granted through a custom break-outboard with PicoZed interfaces. Furthermore, the OPU hosts a SD-card with 8 GB storage capacity.

C. Power Budget

M6P's solar arrays generate approximately 11.65 W during a period of 58.9 min in sunlight out of a total orbital period of 94.6 min. Determining if energy is sufficient during burdensome operations, the power budget should assume a scenario where image acquisition, processing and downlink all happen in the same pass during sunlight. This scenario is shown in Fig. 14 for HYPSO-1 passing over a target area in Lofoten, Norway, and the selected ground stations at NTNU Trondheim, KSAT Svalbard and KSAT Spain.

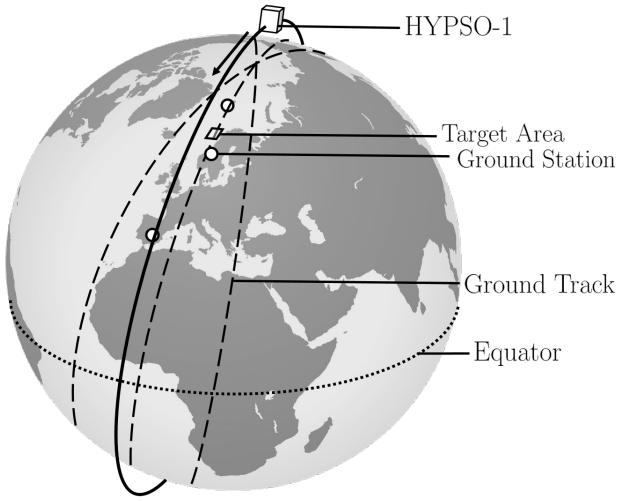

Fig. 14. HYPSO-1 in SSO at 10:25:00 on 28 May 2022. Selected ground stations are marked in white circles. Previous, current and succeeding ground tracks are indicated by dashed lines.

TABLE IV
HYPSO-1 POWER BUDGET

Subsystem	Power (W)	DC (%)	Power Used (W)
Hyperspectral imager	3.675	1.09	0.040
RGB camera	3.375	0.55	0.020
OPU imaging	4.234	1.09	0.046
OPU image processing	4.234	6.69	0.283
OPU-PC transfer	4.234	35.33	1.496
ADCS cruise	3.441	94.72	3.259
ADCS precise	6.331	5.28	0.334
S-band radio RX	4.813	10.57	0.509
S-band radio TX+RX	12.201	10.57	1.290
Other	1.530	100	1.530
Total (+10% margin)			9.688
Generated (effective)			9.861
Remaining			+0.174

Table IV shows the power budget with 5% component margin and the corresponding subsystem duty cycles (DC) that includes booting up. Battery input and output efficiencies are assumed 92% each. The power consumed in OPU, ADCS and S-band radio are separated into more than one operational mode, while "Other" denotes the collective power consumption by FC, EPS, PC and internal bus communications. Naturally, peaks in power are expected during the image acquisition, image processing and downlink. "ADCS precise" indicates preparing and executing the slew maneuver during image acquisition when both the IMU and star-tracker are active, consuming up to 1.5 W each. Adding a 10% system margin results in remaining power of about 174 mW. Enforcing the power budget to remain safe and positive, the allowed duration is set to maximum 6.33 min for onboard image processing and 33.42 min for transferring data from OPU to PC through

CAN. Allowed duration of data transmission through S-band radio is set to 10 min which enables downlinking up to 75 MB of data per orbit.

VI. Onboard image processing architecture

A. Overview

The FPGA-based image processing algorithms on the OPU are key to enable faster download and distribution of data while at the same time relieving HYPSO-1's power budget. The idea behind the image processing architecture is to allow for modular arrangement of algorithms, or pipelines, as illustrated in Fig. 15. The minimal, dimensionality reduction, target detection, and classification on-board image processing pipelines (respectively named MOBIP, DROBIP, TOBIP and COBIP) are designed to generate tailored data products depending on the particular need of the user or operator. All pipelines include image acquisition, time-stamping and binning prior to image processing. It is critical that also satellite and payload telemetry and any other relevant metadata are downlinked together with the processed images, including ADCS and orbit position data collected during image acquisition. Table V shows the size reduction and processing speeds for the suggested algorithms to be employed in the architecture. "Bands/Components" are referred to as spectral bands for raw data and MOBIP, extracted components for DROBIP, a probability map of detected target spectral signatures for TOBIP, and a layer containing classes of spectra for COBIP. A raw hyperspectral datacube of 956×684 spatial pixels and 1080 spectral pixels binned by a factor of $B_\lambda = 9$ times is considered as the starting point for further processing. The data size reduction and processing speed estimates are based on performance reported on state-of-the-art image processing algorithms that have been used on hyperspectral data of similar sizes. Details related to occupation, execution time, operating frequency and latency of the following FPGA-based algorithms can be found in the respective literature on their implementation.

B. Minimal on-board image processing

MOBIP consists of the CCSDS123v1 lossless compression algorithm [71], applied after image acquisition, time-stamping and binning. CCSDS123v1 proposed in [72], [73] offers a measured FPGA core speed of up to 9984 Mbps on HYPSO-1's Zynq-7030 Xilinx PicoZed. With the raw binned image as starting point, a data compression of at least 55.6% is measured as shown in Table V, i.e. a reduction factor of 2.25 times. Without loss of spatial or spectral information, this data product can be independently processed and analyzed further on ground by any user. Furthermore, the CubeDMA, a Direct Memory Access (DMA) solution, is built in the FPGA to ensure efficient stream of hyperspectral images by excluding the Central Processing Unit (CPU) from its critical path of transfer and establishing direct communication between the memory and the dedicated CCSDS123v1 processing core [74].

C. Onboard image processing for tailored data

Given the in-orbit reconfigurability of the FPGA, several suitable algorithms that can be used in DROBIP, TOBIP, COBIP are described here. Some are demonstrated as FPGA-implementations or software/hardware co-designs in relevant hardware, and a few algorithms run in software that need further development for optimized implementations to run on-board.

1) Dimensionality reduction: Dimensionality reduction methods extract the main spectral patterns and remove redundancies from the high-dimensional hyperspectral data. Applying dimensionality reduction as a pre-processing step before any succeeding algorithms increases overall computational efficiency [75], and the practical spatial-spectral features of interest can be used for e.g. studying the water-leaving radiance and atmospheric effects in an observed heterogeneous scene. Shown in Table V, with 20 components chosen, a size reduction rate is estimated to be 92.4% when combined with CCSDS123v1. An optional step before dimensionality reduction can be to apply smile and keystone corrections to prevent intertwining systematic artifacts irrevocably in the data by adjusting the images to account for systematic optical and measurement noise inherent to the hyperspectral imager [76].

A common dimensionality reduction technique is Principal Component Analysis (PCA) which obtains a reduced and de-noised subspace representation of the raw hyperspectral data, assuming a linear model with Gaussian noise [77]. The extracted spatial-spectral information in a scene are contained in only a few principal components instead of several dozens of spectral bands. An FPGA implementation of PCA in Xilinx Virtex-7 XC7VX690T proposed in [78] is reported to obtain computational speed of 4.17 s when used to extract 24 principal components from an Airborne visible/infrared imaging spectrometer (AVIRIS) image of Jasper Ridge Biological Preserve, California, with 614×512 spatial pixels and 224 spectral channels, and is fast enough to process a stream of hyperspectral images in real-time. According to [79], an adaptive bilinear PCA-based On-the-Fly Processing (OTFP) algorithm may sequentially process streaming blocks of data instead of analyzing the whole dataset at the end of image acquisition. Although in Matlab, its reported computational speed is 300.2 s for obtaining 3 principal components from a 16-bit hyperspectral image of 1000×245 spatial pixels and 450 spectral channels, however higher speed is expected for an FPGA implementation. An alternative method to PCA, the Extended Multiplicative Signal Correction (EMSC) estimates a de-noised subset of relevant spectra using a linear statistical model of observations with approximated light absorbance and scattering [80]. A software/hardware co-design of EMSC on a Zedboard development platform with ARM Cortex-A9 processor measures a computational time of 3.81 seconds when applied on a 16-bit hyperspectral datacube with 500×500 spatial pixels and 50 spectral channels.

2) Target detection: Hyperspectral images of heterogeneous scenes are amenable to spectral-based target detection because of their numerous spectral bands [81], [82]. An effective use of target detection in hyperspectral imagery requires a

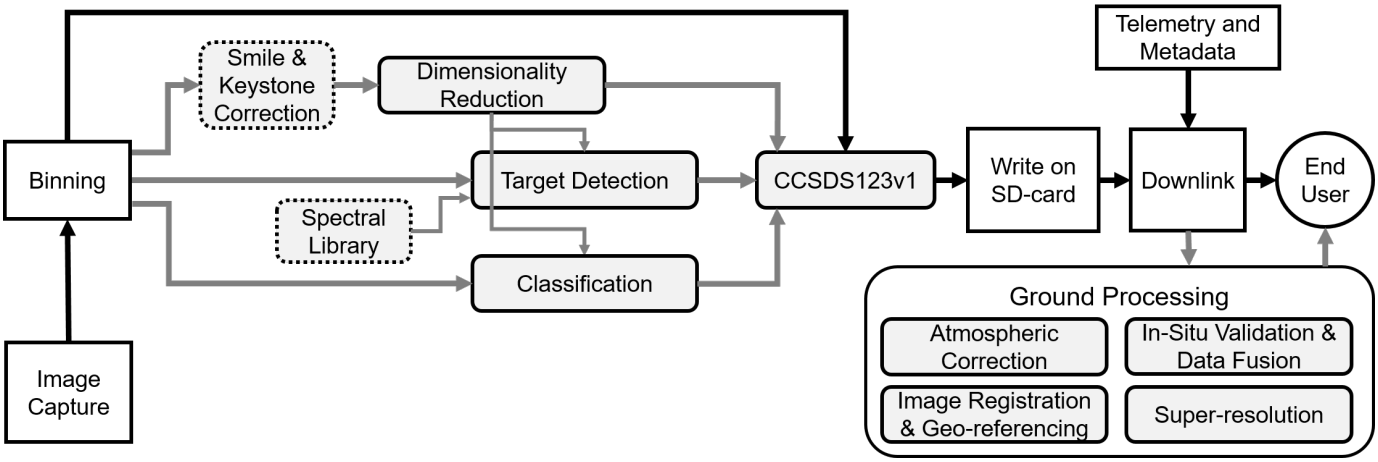

Fig. 15. Block diagram of the proposed imaging processing pipelines. In order, the hyperspectral images are captured, binned, processed at chosen level, stored on SD-card and downlinked together with collected telemetry and metadata. Depending on the downlinked data product, additional ground-based processing and fine-tuning can be applied before distribution to end user. In-situ validation and data fusion with other remote sensing data are critical aspects the HYPSO-1 data validation. Black arrows indicate the minimal onboard processing pipeline while gray arrows are the alternative routes for tailored data products.

TABLE V
HYPERSPECTRAL DATA PRODUCTS FOR $N_x \times N_y = 956 \times 684$ SPATIAL PIXELS

Level	Bands/Components	Pixel size (bits)	Total (MB)	Reduction (%)	Speed (Mbps)
Raw Binned (at $B_\lambda = 9$)	120	16	156.94	-	-
CCSDS123 (MOBIP)	120	16	69.75	55.6	6260^a
PCA (DROBIP)	20	16	11.89	92.4	268.6^b
OTFP (DROBIP)	20	16	11.89	92.4	7^c
EMSC (DROBIP)	20	16	11.89	92.4	54.5^d
Target detection (TOBIP)	1	16	1.308	99.2	903.1^d
Classification - 16 classes (COBIP)	1	4	0.331	99.8	53.2^c
Classification - 256 classes (COBIP)	1	8	0.711	99.6	53.2^c

a : measured on Zynq-7030 Xilinx FPGA flight hardware on OPU.
b : estimated from Xilinx Virtex-7 XC7VX690T FPGA-based software/hardware co-design tests on similar hyperspectral data size.
c : estimated from software implementation test on similar hyperspectral data size.
d : estimated from Zynq-7000 FPGA-based software/hardware co-design tests on similar hyperspectral data size.

set of a-priori known target spectra and high spatial resolution is desired to reduce the effects of spectral mixing in the spatial pixels. Target detection generates a probability map of target spectral signatures across the image in the spatial domain, resulting in a two-dimensional data product per chosen number of signatures as indicated in Table V. As an example, only one target signature is chosen such that the size of the two-dimensional map is $1 \times 956 \times 684 \times 16$ bits $= 1.308$ MB, i.e. a size reduction of approximately 99.2% of the original data. Due to the small data size, the reduction for target detection in Table V is assumed to not include lossless compression with CCSDS123v1.

Proposed in [83], the target detection module supports Constrained Energy Minimization (CEM), Adjusted Spectral Matched Filter (ASMF) and modified Adaptive Cosine Estimator (ACE) detectors to determine the likelihood of specific spectral signatures in a spatial pixel. For real-time computation on a stream of hyperspectral images, dimensionality reduction should be applied as a pre-processing step. For software/hardware co-design of modified ACE algorithm on a Zedboard development platform with ARM Cortex-A9 processor, the computational time is reported to be 3.29 s for an input of HyMap 16-bit hyperspectral datacube of 224000 spatial pixels and 16 principal components given PCA pre-processing [84]. A computational time of 0.5 s is reported for FPGA-implementation of modified ACE algorithm on a Zynq-7035 SoC (Kintex-7) applied on the complete HyMap datacube with 126 spectral bands without PCA pre-processing [83], which is used as benchmark estimate in Table V.

3) Classification: Using a spatial-spectral classification framework, the spatial pixels in a hyperspectral image can be separated into different classes based on spectral signatures [85]. One of many such classification techniques that are suitable for FPGA-implementation is the Fast Spectral Clustering (FSC), a graph-based unsupervised method that does not require training data [86], [87]. Indicated in Table V, it is possible to represent each pixel or layer with a 4 bit integer for fewer than 16 classes, whereas 256 classes can be represented with 8 bits. The size of 16 class signatures with 120 spectral bands per signature is $16 \times 120 \times 16$ bits $= 0.0038$ MB and for 256 class signatures the size is $256 \times 120 \times 16$ bits $= 0.06144$ MB. These auxiliary data products are added to the classification map with size of $1 \times 956 \times 684 \times 4$ bits $= 0.327$ MB for 16 classes and $1 \times 956 \times 684 \times 8$ bits $= 0.654$ MB for 256 classes. The estimated data size reduction is 99.8% and 99.6%, respectively. Due to the small data sizes, the reductions for classification in Table V are assumed to not include lossless compression with CCSDS123v1.

The computational speed for a Nystrøm Extension Clustering version of FSC, described in [86], is estimated to be about $245.8\ \mathrm{Mbps}$ based on a Matlab implementation that resulted in $1.62\ \mathrm{s}$ used for providing 16 classes from a 16-bit AVIRIS image of Salinas Valley, California, with 512×217 pixels and 224 spectral bands. Even higher speed is expected for a software/hardware co-design of FSC on FPGA. An alternative to FSC is the potentially more accurate Clustering using Binary Partition Trees (CLUS-BPT) framework which integrates embedded hyperspectral data segmentation, region modeling, feature extraction by PCA and clustering [88]. Its reported computation time in Matlab is $7.48\ \mathrm{s}$ for the same AVIRIS image. However, FSC generally outperforms the CLUS-BPT in terms of computational time for an input image with large spatial dimensions. As a worst case in Table V, the estimated processing speed is therefore assumed to be $53.2\ \mathrm{Mbps}$ based on CLUS-BPT. Naturally, as with any other onboard processing algorithms, cropping the images in the spatial domain to rather focus on specific regions will improve the processing latency in classification.

D. Discussion on advanced algorithms

Given the FPGA reconfigurability, other relevant algorithms beyond those discussed may be uploaded to the OPU in-orbit if potential maturity is reached. Generally, the algorithms should first be rigorously tested on ground with careful validation of processing characteristics such as speed, reliability and acceptable accuracy resulting in the data. Relevant algorithms include image registration, geo-referencing, atmospheric correction and super-resolution which may improve the accuracy in target detection and classification. However, these algorithms are generally too computationally intensive and complex for onboard implementation and real-time use. Further studies, development and testing are required.

1) Image registration: Image registration is the determination of relative separation between individual pixels, sometimes named orthorectification. Such algorithms are in general too computationally expensive for on-board applications [89]. A simpler ray-tracing method can be adapted for on-board implementation, which has been prototyped for joint registration and geo-referencing, similar to the one described in [90].

2) Geo-referencing: The benefit in onboard geo-referencing lies in directly downlinking the latitude and longitude coordinates of pixels with results from target detection or classification. This requires immediate inputs of time-synchronized ADCS and navigation data. For ground use, instead of downlinking the whole data product from e.g. target detection or classification, it is possible to transfer only the relevant spatial pixel indices to be geo-referenced. This results in much smaller data size and latency, and in-situ agents nearby HYPSO-1's observed area can therefore quickly be commanded to travel to these coordinates for closer inspection.

3) Super-resolution: Super-resolution algorithms can be adapted to enhance the spatial resolution in images as described in [91], and thereby improve the radiometric and geometric accuracy. Super-resolution prototypes require a measurement process, e.g. determining the point-spread function, to infer higher spatial resolution in the image [92], [93], which are based on methods from multi-frame super-resolution [94], [95]. Although these types of algorithms can improve the image spatial resolution, they are susceptible to noise, quantization, compression and inaccuracies in the estimate of the point spread function [96], [97]. Prior-based super-resolution techniques, such as sparse image representations [98] and convolutional neural nets [99], [100], namely overcome the limitations in measurement-based techniques by supplementing input pixels with expectations of hyperspectral image statistics. Other methods involve using multispectral-hyperspectral image fusion [101], [102] and super-resolution based on dimensionality reduction [103].

An FPGA-implementation of a Richardson-Lucy (RL) deconvolution algorithm on Xilinx Zynq-7020 Zedboard with two ARM Cortex-A9 cores proposed in [104], has been successfully applied on a hyperspectral data, where a computational time of $1.06\ \mathrm{ms}$ is reported per iteration when processing a band with size of 150×640 pixels by using kernel size of 9×9 pixels. Corresponding software/hardware co-design of the deconvolution algorithm is proposed in [105].

4) Atmospheric Correction: Removing atmospheric effects before dimensionality reduction, target detection or classification, can improve the accuracy and efficiency in extracting or detecting relevant water-leaving signals. The purpose of atmospheric correction is to identify the terms in (6) that contribute to the total ToA radiance, $L_{\text{total}}^{\text{ToA}}$, and predict the actual water-leaving radiance component, L_{water}, which may further contain the optical properties of water constituents, e.g. chlorophyll.

Many ground-based atmospheric correction schemes work well for open ocean waters for multispectral data [56], [106], [107], [108], and good performance has also been shown for hyperspectral images of coastal waters [109]. Traditional atmospheric correction methods are generally built on the radiative transfer model [48], but they are not designed for onboard real-time applications due to complexity and computational expense. Without contemporary empirical or ground truth data, they can also be prone to over- or undercorrection of the radiance terms in (6), resulting in significant radiometric inaccuracies for highly variable coastal waters and an unpredictable atmosphere. On the other hand, effective non-deterministic atmospheric correction methods using machine learning, e.g. neural networks, have regularly been employed and are considered to be robust given a proper set of training data [108]. If trained hyperspectral images or ground truth data are unavailable, simulation tools such as Accurate Radiative Transfer (AccuRT) [110], based on a coupled atmosphere-ocean radiative transfer model, could simulate heterogeneous scenes of complex water and atmosphere to be used for training [111]. A suitable on-board FPGA implementation of atmospheric correction methods needs further investigation.

E. Dynamic Reconconfiguration

Using FPGAs can overcome the limited hardware resources onboard a small-satellite and the increasing performance requirements for onboard processing in terms of processing

TABLE VI
PERFORMANCE FOR SELECTED HYPERSPECTRAL IMAGER MODES

Type	Mode A	Mode B	Mode C	Mode D	Mode E
ADCS Mode	Slew	Slew	Slew	Nadir	Nadir
AoI (pixels)	1080×684	1080×684	1080×1194	1080×1194	1936×1216
Binning, B_λ (pixels)	9	18	9	9	1
Spectral range (nm)	$387 - 801$	$387 - 801$	$387 - 801$	$387 - 801$	$220 - 967$
Spectral bands	120	60	120	120	215
Bandpass $\Delta\lambda$ (nm)	3.33	6.67	3.33	3.33	3.33
Frame rate FPS	18	12	12	12	10
Exposure time, τ (ms)	51	79	79	79	96
Scan duration (s)	53.08	53.08	57.00	9.19	1.00
Number of frames	956	637	685	111	10
Scan distance, along-track (km)	40.08	40.08	69.97	69.97	7.60
Swath width (km)[a]	40.08	40.08	69.97	69.97	69.97
Spatial resolution, along-track (m)[a,b]	553	582	618	1101	1231
Spatial resolution, cross-track (m)[a,b]	58.60	58.60	58.60	58.60	58.60
SGSD, along-track (m)	57.6	86.3	124.1	634.4	761.3
$\text{SNR}_{\text{water},[B_\lambda,1]}$ @470 nm[a]	158.1	196.3	197.4	197.4	217.9
Data size, raw (MB)	156.94	52.28	196.29	31.81	4.71
Data size, MOBIP (MB)	69.75	23.24	87.24	14.14	2.09
Onboard processing time (s)[c]	5.8	1.9	7.2	1.2	0.2
OPU-PC transfer time (s)[c]	1924.1	641	390	2406.7	57.7
Downlink time (s)[d]	558.0	185.9	697.9	113.1	16.7
Data size, DROBIP (MB)[e]	11.62	7.75	14.54	2.36	0.22
Onboard processing time (s)[e]	5.6	2.2	7.0	1.1	0.2
OPU-PC transfer time (s)[c]	320.7	213.7	401.1	65.0	6.0
Downlink time (s)[d]	93.0	62.0	116.3	18.8	1.7
Data size, TOBIP (MB)[e]	1.31	0.87	1.64	0.27	0.02
Onboard processing time (s)[e]	8.9	3.0	11.1	1.8	0.29
OPU-PC transfer time (s)[c]	36.1	24.0	45.1	7.3	0.7
Downlink time (s)[d]	10.5	7.0	13.1	2.1	0.2
Data size, COBIP (MB)[e]	0.33	0.22	0.41	0.07	0.01
Onboard processing time (s)[e]	23.6	7.9	29.6	4.8	0.8
OPU-PC transfer time (s)[c]	9.1	6.1	11.4	1.9	0.4
Downlink time (s)[d]	2.6	1.8	3.3	0.6	0.1

a: viewing at nadir.
b: the spatial resolution in one frame, not the final image resolution using e.g. image registration and super-resolution.
c: includes time used for running on memory in the OS and writing data to SD-card at 100 Mbps.
d: total time required for 1 Mbps downlink data rate with S-band radio.
e: estimated based on Table V.

TABLE VII
MODE A DATA LATENCY FOR HYPSO-1 ON EXAMPLE DATE 28 MAY 2022

	MOBIP	(69.75 MB)	DROBIP	(11.62 MB)	TOBIP	(1.31 MB)	COBIP	(0.33 MB)
Sequence	Start time	Duration (s)	Start time	Duration (s)	Start time	Duration (s)	Start time	Duration (s)
Orbit 1								
Image acquisition	10:29:40.0	53.1	10:29:40.0	53.1	10:29:40.0	53.1	10:29:40.0	53.1
Onboard processing	10:30:33.1	5.8	10:30:33.1	5.6	10:30:33.1	1.5	10:30:33.1	23.6
OPU to PC transfer	10:30:38.9	1924.1	10:30:38.7	320.7	10:30:34.6	36.1	10:30:56.7	9.1
Downlink NTNU	-	-	-	-	10:31:10.7	10.5	10:31:05.8	2.6
Downlink KSAT Spain	-	-	10:35:59.4	93.0	-	-	-	-
Cruise	11:02:43.0	434.7	-	-	-	-	-	-
Eclipse	11:09:56.7	2145.0	-	-	-	-	-	-
Orbit 2								
Cruise	11:45:42.0	630.0	-	-	-	-	-	-
Downlink KSAT Svalbard	11:56:12.0	276.0	-	-	-	-	-	-
Downlink NTNU	12:00:48.0	282.0	-	-	-	-	-	-
Total latency (min)		95.85		7.87		1.69		1.47

TABLE VIII
MODE A DATA LATENCY FOR HYPSO-1 WITHOUT CAN OVERHEAD ON EXAMPLE DATE 28 MAY 2022

	MOBIP	(69.75 MB)	DROBIP	(11.62 MB)	TOBIP	(1.31 MB)	COBIP	(0.33 MB)
Sequence	Start time	Duration (s)	Start time	Duration (s)	Start time	Duration (s)	Start time	Duration (s)
Image acquisition	10:29:40.0	53.1	10:29:40.0	53.1	10:29:40.0	53.1	10:29:40.0	53.1
Onboard processing	10:30:33.1	5.8	10:30:33.1	5.6	10:30:33.1	1.5	10:30:33.1	23.6
Downlink NTNU	10:30:38.9	316.0	10:30:38.7	93.0	10:30:34.6	10.5	10:30:56.7	2.6
Downlink KSAT Spain	10:35:54.9	242.0	-	-	-	-	-	-
Total latency (min)		8.62		2.53		1.09		1.32

complexity and spatial-spectral resolution in hyperspectral data. Using Dynamic Reconfiguration (DR) on FPGAs, reconfigurable solutions obtain the needed flexibility and allow changes and adaptation of the onboard processing In HYPSO-1, the DR can be used to increase resource utilization by switching between different processing pipelines and for functional updates and upgrades in each pipeline that are uplinked from the ground. An advanced ability of modern FPGAs is Dynamic Partial Reconfiguration (DPR) that reprograms portions of the FPGA, while the rest of the system continues to operate. The DPR allows time-multiplexing of mutually time-exclusive algorithms/steps on a finer scale of the available resources and is characterized by shorter reconfiguration times since FPGA configuration time is directly proportional to the configuration bitstream size. The DPR can also be used for applications such as mitigation and recovery from single-event upsets (SEU) and for real-time dynamic scenario-based adaptive image processing. Furthermore, the OPU also has a "golden image" that enables booting a previous version of a steady on-board processing configuration. The OPU will automatically revert to the "golden image" in case of corruption or unwanted updates or upgrades that have been uploaded from ground.

F. Ground Support

Indicated at bottom right in Fig. 15, some of the algorithms should operate on the ground at all times to (a) adjust, fine-tune and prepare data for end users; (b) assist in in-orbit calibration of the hyperspectral imager; and (c) rigorously test accuracy and reliability in algorithm updates before uploading them to the satellite for onboard image processing. Advanced modules such as image registration, geo-referencing, atmospheric correction and super-resolution are dedicated for use on ground because they require access to prompt reference libraries and are computationally expensive. In-orbit upgrades, or at least future missions, may include versions of the aforementioned algorithms only if maturity is demonstrated on ground. Apart from suitable implementations before launch, alternative prototype algorithms for dimensionality reduction, target detection and classification are also tested on ground first.

G. Data latency in typical HYPSO-1 operations

Table VI shows HYPSO's remote sensing performance for selected hyperspectral imager modes and corresponding size and latency for data products obtained from MOBIP, PCA-based DROBIP, TOBIP with one twodimensional map and COBIP with 16 classes. For each pipeline, the assumptions are based on the chosen spectral channels, pixel size in bits, reduction factors and processing speeds stated in Table V, but with extended results for other datacube sizes. The ADCS modes with slew maneuvers are set with starting angle $\theta_0 = 20^\circ$ and final angle $\theta_f = -20^\circ$ at $\omega_y = -0.754^\circ/\mathrm{s}$ and are assumed to have no attitude control and knowledge errors. The SNR is calculated using the ToA water-leaving radiance based on data from MOBY as described in Section III-C.

Modes A and B provide higher spatial resolution but narrower FoV for a chosen observed area size of approximately $40\ \mathrm{km}$ by $40\ \mathrm{km}$, while Modes C and D provide coarser spatial resolution and wider FoV for a chosen target area size of approximately $70\ \mathrm{km}$ by $70\ \mathrm{km}$. Modes A, B, C and D use 1080 out of 1936 spectral pixels to cover the relevant spectral range of $400 - 800\ \mathrm{nm}$. Mode E is dedicated for diagnostics and in-orbit calibration during commissioning phase. "Onboard processing time", "OPU-PC transfer time" and "Downlink time" are the durations needed for image processing for selected pipeline, completing the data transfer between OPU to PC at speeds of up to $290\ \mathrm{kbps}$ and completing the data downlink to ground through S-band radio at a bandwidth of $1\ \mathrm{Mbps}$, respectively. It is also assumed that the onboard data is written to the SD-card at $100\ \mathrm{Mbps}$ which is included in the onboard processing time.

The results from Table VI are put into the context of a typical mission scenario where HYPSO-1 uses Mode A to observe a $40\ \mathrm{km} \times 40\ \mathrm{km}$ near Lofoten, Norway, then immediately aims to downlink a selected data product to ground stations at NTNU, KSAT Svalbard and KSAT Spain with respective elevation angles assumed to be 5°, 2° and 8°. Using simulated orbit propagator in Analytical Graphics, Inc., (AGI) Systems Toolkit (STK) with epoch date set to 28 May 2022, results are shown in Tables VII with OPU-PC overhead and VIII without the overhead. A dash indicates that the operation is not available or necessary. "Cruise" means that HYPSO-1 is only harvests solar energy and "Eclipse" means that it is in the Earth's shadow. With overhead in OPU-PC transfer, all except for MOBIP data product can be downloaded in less than one orbit, or specifically less than $10\ \mathrm{min}$. All data products are available in less than $10\ \mathrm{min}$ without the overhead.

Regarding the OPU-PC transfer overhead, the current hardware and software architecture in HYPSO-1 is limited by the communication interface between the OPU and the PC due to data transfer over a CAN network with a data rate of about $300\ \mathrm{kbps}$, which negatively impacts the overall latency for larger data sizes as indicated in Table VII. In future missions, the physical interface could be replaced with a data bus capable of higher data rates, for example Ethernet or RS-422, which would involve spending much less time by downlinking directly from the OPU, and better latency can be potentially achieved as shown in Table VIII.

VII. Conclusions

Following the advancements in miniaturization, image processing algorithms and sensor technology, the mission and system design of HYPSO-1 shows that pushbroom hyperspectral imaging combined with FPGA-based on-board image processing on a nano-satellite, can enable ocean color data products with high spatial and spectral resolution and low data latency to meet the user needs for operational coastal environment monitoring. The imager design, HYPSO-1's remote sensing approach and on-board software grants flexible trade-offs to be made between image spatial resolution, spectral resolution and SNR. The chosen FPGA-based CCSDS123v1

lossless compression, dimensionality reduction, target detection, and classification algorithms may reduce the data size significantly without losing crucial information. In contrary to using rigorous data processing and analysis on ground, the smaller data products can be made available within minutes after observation. This enables quick download of tailored data products that may satisfy immediate needs of end users, as such it could for example allow better mitigation for potential damage from Harmful Algal Blooms when early detection and warning are needed. Based on lessons learned from the HYPSO-1 operations, the goal is to iterate and enhance the design of the hyperspectral imager, attitude determination and control system, satellite communications architecture, and the on-board image processing algorithms for future missions. After launch, the HYPSO-1 mission aims to determine the efficacy in quickly providing high-resolution hyperspectral data from small-satellites for ocean color applications.

ACKNOWLEDGMENTS

The authors would like to thank Kanna Rajan at Faculty of Engineering, University of Porto, for his substantial contribution to the HYPSO-1 mission design and motivation towards establishing a small-satellite constellation for oceanography. Authors also thank Liane S. Guild, Stephen Dunagan and Chad Frost at NASA Ames Research Center, Raphael M. Kudela at the Ocean Sciences Department, University of California Santa Cruz, Richard P. Stumpf at National Oceanic and Atmospheric Administration (NOAA), and Ajit Subramaniam at the Lamont-Doherty Observatory, Columbia University, for their guidance and valuable discussions on remote sensing and mission development. Authors would also like to thank Geir Johnsen at Department of Biology, NTNU, for his review on requirements in ocean color remote sensing, Torbjørn Skauli at Norwegian Defense Research Establishment (FFI) for his review on spectroscopy, Fernando Aguado Agelet at the Department of Telecommunications Engineering, University of Vigo, and Cecilia Haskins at Department of Mechanical Engineering, NTNU, for their input on systems engineering in the project, Annette Stahl and Dennis Langer at Department of Engineering Cybernetics, NTNU, for their strong inputs on image processing, Egil Eide and Gara Quintana Diaz at Department of Electronic Systems, NTNU, for their help on radio communications, and Harald Martens, João Fortuna and Petter Rossvoll at IdleTechs for their recommendations on dimensionality reduction of hyperspectral data. Finally, authors are grateful for the participation of NanoAvionics and their continuous feedback throughout the project.

REFERENCES

[1] G. Johnsen, M. A. Moline, L. H. Pettersson, J. Pinckney, D. V. Pozdnayakov, E. S. Egeland, and O. M. Schofield, "Optical monitoring of phytoplankton bloom pigment signatures," in *Phytoplankton Pigments: Characterization, Chemotaxonomy and Applications in Oceanography*, S. Roy, C. A. Llewellyn, E. S. Egeland, and G. Johnsen, Eds. Cambridge University Press, 2011, ch. 14, pp. 538–606.

[2] IOCCG, *Phytoplankton Functional Types from Space*, S. Sathyendranath, Ed., Reports of the International Ocean-Colour Coordinating Group, No. 15, IOCCG: Dartmouth, NS, Canada, 2014.

[3] D. Blondeau-Patissier, J. F. Gower, A. G. Dekker, S. R. Phinn, and V. E. Brando, "A review of ocean color remote sensing methods and statistical techniques for the detection, mapping and analysis of phytoplankton blooms in coastal and open oceans," *Prog. Oceanogr.*, vol. 123, pp. 123–144, 2014.

[4] T. Kutser, L. Metsamaa, N. Strombeck, and E. Vahtmae, "Monitoring cyanobacterial blooms by satellite remote sensing," *Estuar. Coast. Shelf Sci.*, vol. 67, pp. 303–312, 2006.

[5] G. Johnsen, K. T. Z. Volent, and E. Sakshaug, "Time series of harmful and benign phytoplanktonblooms in northwest European waters using the Seawatch buoy system," in *Monitoring Algal Blooms: New Technologies for Detecting Large-Scale Environmental Change*. Springer-Verlag and Landes Bioscience, 1997, ch. 6, pp. 113–141.

[6] G. Johnsen, O. Samset, L. Granskog, and E. Sakshaug, "In vivo absorption characteristics in 10 classes of bloom-forming phytoplankton: taxonomic characteristics and responses to photoadaptation by means of discriminant and HPLC analysis," *Mar. Ecol. Prog. Ser.*, vol. 105, pp. 149–157, 1994.

[7] D. A. Jessup, M. A. Miller, J. P. Ryan, H. M. Nevins, H. A. Kerkering, A. Mekebri, D. B. Crane, T. A. Johnson, and R. M. Kudela, "Mass Stranding of Marine Birds Caused by a Surfactant-Producing Red Tide," *PLoS One*, vol. 4, no. 2, pp. 1–8, 2009.

[8] T. D. Dickey and R. R. Bidigare, "Interdisciplinary oceanographic observations: the wave of the future," *Sci. Mar.*, vol. 69, pp. 23–42, 2005.

[9] IOCCG, *Remote Sensing in Fisheries and Aquaculture*, M.-H. Forget, V. Stuart, and T. Platt, Eds., Reports of the International Ocean-Colour Coordinating Group, No. 8, IOCCG: Dartmouth, NS, Canada, 2009.

[10] C. O. Davis, J. Bowles, R. A. Leathers, D. Korwan, T. V. Downes, W. A. Snyder, W. J. Rhea, W. Chen, J. Fisher, W. P. Bissett, and R. A. Reisse, "Ocean PHILLS hyperspectral imager: design, characterization, and calibration," *Opt. Express*, vol. 10, no. 4, pp. 210–221, 2002.

[11] M. R. Corson, D. R. Korwan, R. L. Lucke, W. A. Snyder, and C. O. Davis, "The Hyperspectral Imager for the Coastal Ocean (HICO) on the International Space Station," in *IGARSS 2008 - 2008 IEEE Int. Geosci. Remote Sens. Symp.*, vol. 4, July 2008, pp. 101–104.

[12] B.-C. Gao, M. J. Montes, C. O. Davis, and A. F. Goetz, "Atmospheric correction algorithms for hyperspectral remote sensing data of land and ocean," *Remote Sens. Environ.*, vol. 113, pp. S17 – S24, 2009.

[13] E. J. Knight and G. Kvaran, "Landsat-8 Operational Land Imager Design, Characterization and Performance," *Remote Sens.*, vol. 6, no. 11, pp. 10 286–10 305, 2014.

[14] M. Aguirre, B. Berruti, J.-L. Bezy, M. Drinkwater, F. Heliere, U. Klein, C. Mavrocordatos, P. Silvestrin, B. Greco, and J. Benveniste, "Sentinel-3 - the ocean and medium-resolution land mission for GMES operational services," *ESA Bull.*, vol. 131, pp. 24–29, Aug 2007.

[15] F. E. Muller-Karger, E. Hestir, C. Ade, K. Turpie, D. A. Roberts, D. Siegel, R. J. Miller, D. Humm, N. Izenberg, M. Keller, F. Morgan, R. Frouin, A. G. Dekker, R. Gardner, J. Goodman, B. Schaeffer, B. A. Franz, N. Pahlevan, A. G. Mannino, J. A. Concha, S. G. Ackleson, K. C. Cavanaugh, A. Romanou, M. Tzortziou, E. S. Boss, R. Pavlick, A. Freeman, C. S. Rousseaux, J. Dunne, M. C. Long, E. Klein, G. A. McKinley, J. Goes, R. Letelier, M. Kavanaugh, M. Roffer, A. Bracher, K. R. Arrigo, H. Dierssen, X. Zhang, F. W. Davis, B. Best, R. Guralnick, J. Moisan, H. M. Sosik, R. Kudela, C. B. Mouw, A. H. Barnard, S. Palacios, C. Roesler, E. G. Drakou, W. Appeltans, and W. Jetz, "Satellite sensor requirements for monitoring essential biodiversity variables of coastal ecosystems," *Ecol. Appl.*, vol. 28, no. 3, pp. 749–760, 2018.

[16] I. Ogashawara, "The Use of Sentinel-3 Imagery to Monitor Cyanobacterial Blooms," *Environments*, vol. 6, no. 6, 60, 2019.

[17] F. Ortenberg, *Hyperspectral Sensor Characteristics*. Hyperspectral Remote Sensing of Vegetation, 2011, pp. 39–68.

[18] J. L. Wolny, M. C. Tomlinson, S. Schollaert Uz, T. A. Egerton, J. R. McKay, A. Meredith, K. S. Reece, G. P. Scott, and R. P. Stumpf, "Current and Future Remote Sensing of Harmful Algal Blooms in the Chesapeake Bay to Support the Shellfish Industry," *Front. Mar. Sci.*, vol. 7, 2020.

[19] M. Soukup, J. Gailas, D. Fantin, A. Jochemsen, C. Aas, P. J. Baeck, L. Benhadj, S. Livens, B. Delauré, M. Menenti, B. G. H. Gorte, S. E. Aria Hosseini, M. Esposito, and C. N. van Dijk, "HyperScout: Onboard Processing of Hyperspectral Imaging Data on a Nanosatellite," in *Small Satellites, System and Services Symposium (4S), Valletta, Malta*, 2016.

[20] H. Dierssen, G. B. McManus, A. Chlus, D. Qiu, B.-C. Gao, and S. Lin, "Space station image captures a red tide ciliate bloom at high spectral and spatial resolution," *Proc. Natl. Acad. Sci.*, vol. 112, no. 48, pp. 14 783–14 787, 2015.

[21] L. Guanter, H. Kaufmann, K. Segl, S. Foerster, C. Rogass, S. Chabrillat, T. Kuester, A. Hollstein, G. Rossner, C. Chlebek, C. Straif, S. Fischer, S. Schrader, T. Storch, U. Heiden, A. Mueller, M. Bachmann, H. Mühle, R. Müller, M. Habermeyer, A. Ohndorf, J. Hill, H. Buddenbaum, P. Hostert, S. Van der Linden, P. J. Leitão, A. Rabe, R. Doerffer, H. Krasemann, H. Xi, W. Mauser, T. Hank, M. Locherer, M. Rast, K. Staenz, and B. Sang, "The EnMAP Spaceborne Imaging Spectroscopy Mission for Earth Observation," *Remote Sens.*, vol. 7, no. 7, pp. 8830–8857, 2015.

[22] C. Mielke, N. Boesche, C. Rogass, H. Kaufmann, C. Gauert, and M. de Wit, "Spaceborne Mine Waste Mineralogy Monitoring in South Africa, Applications for Modern Push-Broom Missions: Hyperion/OLI and EnMAP/Sentinel-2," *Remote Sens.*, vol. 6, no. 8, pp. 6790–6816, 2014.

[23] J. Pearlman, P. Barry, C. Segal, J. Shepanski, D. Beiso, and S. Carman, "Hyperion, a Space-Based Imaging Spectrometer," *IEEE Trans. Geosci. Remote Sens.*, vol. 41, pp. 1160 – 1173, 2003.

[24] P. J. Werdell, M. J. Behrenfeld, P. S. Bontempi, E. Boss, B. Cairns, G. T. Davis, B. A. Franz, U. B. Gliese, E. T. Gorman, O. Hasekamp, K. D. Knobelspiesse, A. Mannino, J. V. Martins, C. R. McClain, G. Meister, and L. A. Remer, "The Plankton, Aerosol, Cloud, Ocean Ecosystem Mission: Status, Science, Advances," *Bull. Am. Meteorol. Soc.*, vol. 100, no. 9, pp. 1775–1794, 2019.

[25] Y. Liu, D. Sun, X. Hu, X. Ye, Y. Li, S. Liu, K. Cao, M. Chai, W. Zhou, J. Zhang, Y. Zhang, W. Sun, and L. Jiao, "The Advanced Hyperspectral Imager: Aboard China's GaoFen-5 Satellite," *IEEE Geosci. Remote Sens. Mag.*, vol. 7, no. 4, pp. 23–32, 2019.

[26] D. Li, M. Wang, and J. Jiang, "China's high-resolution optical remote sensing satellites and their mapping applications," *Geo. Spat. Inf. Sci.*, 2020.

[27] A. Villafranca, J. Corbera, F. Martín, and J. F. Marchan, "Limitations of Hyperspectral Earth Observation on Small Satellites," *Journal of Small Satellites*, vol. 1, no. 1, pp. 19–29, 2012.

[28] M. N. Sweeting, "Modern Small Satellites-Changing the Economics of Space," *Proc. IEEE*, vol. 106, no. 3, pp. 343–361, 2018.

[29] E. Prentice, M. E. Grøtte, F. Sigernes, and T. A. Johansen, "Design of hyperspectral imager using COTS optics for small satellite applications," in *Int. Conf. Space Opt. - ICSO 2021*, 2021.

[30] F. Sigernes, M. Syrjäsuo, R. Storvold, J. Fortuna, M. E. Grøtte, and T. A. Johansen, "Do it yourself hyperspectral imager for handheld to airborne operations," *Opt. Express*, vol. 26, no. 5, pp. 6021–6035, 2018.

[31] A. G. C. Guerra, F. Francisco, J. Villate, F. Agelet, O. Bertolami, and K. Rajan, "On small satellites for oceanography: A survey," *Acta Astronaut.*, vol. 127, pp. 404–423, 2016.

[32] J. Praks, P. Niemelä, A. Näsilä, A. Kestilä, N. Jovanovic, B. Riwanto, T. Tikka, H. Leppinen, R. Vainio, and P. Janhunen, "Miniature Spectral Imager in-Orbit Demonstration Results from Aalto-1 Nanosatellite Mission," in *IGARSS 2018 - 2018 IEEE Int. Geosci. Remote Sens. Symp.*, July 2018, pp. 1986–1989.

[33] M. Guelman and F. Ortenberg, "Small satellite's role in future hyperspectral Earth observation missions," *Acta Astronaut.*, vol. 64, no. 11, pp. 1252–1263, 2009.

[34] A. George and C. Wilson, "Onboard Processing With Hybrid and Reconfigurable Computing on Small Satellites," *Proc. IEEE*, vol. 106, pp. 458–470, 2018.

[35] S. Lopez, T. Vladimirova, C. Gonzalez, J. Resano, D. Mozos, and A. Plaza, "The Promise of Reconfigurable Computing for Hyperspectral Imaging Onboard Systems: A Review and Trends," *Proc. IEEE*, vol. 101, no. 3, pp. 698–722, 2013.

[36] L. Sterpone, M. Porrmann, and J. Hagemeyer, "A Novel Fault Tolerant and Runtime Reconfigurable Platform for Satellite Payload Processing," *IEEE Trans. Comput.*, vol. 62, no. 8, pp. 1508–1525, 2013.

[37] C.-I. Chang, *Hyperspectral Imaging: Techniques for Spectral Detection and Classification*. New York: Kluwer Academic, 2003.

[38] J. C. Harsanyi and C. I. Chang, "Hyperspectral image classification and dimensionality reduction: an orthogonal subspace projection approach," *IEEE Trans. Geosci. Remote Sens.*, vol. 32, no. 4, pp. 779–785, 1994.

[39] R. M. Kudela, S. L. Palacios, D. C. Austerberry, E. K. Accorsi, L. S. Guild, and J. Torres-Perez, "Application of hyperspectral remote sensing to cyanobacterial blooms in inland waters," *Remote Sens. Environ.*, vol. 167, pp. 196 – 205, 2015.

[40] K. Davidson, D. M. Anderson, M. Mateus, B. Reguera, J. Silke, M. Sourisseau, and J. Maguire, "Forecasting the risk of harmful algal blooms," *Harmful Algae*, vol. 53, pp. 1–7, 2016.

[41] IOCCG, *Mission Requirements for Future Ocean-Colour Sensors*, C. R. McClain and G. Meister, Eds., Reports of the International Ocean-Colour Coordinating Group, No. 13, IOCCG: Dartmouth, NS, Canada, 2012.

[42] L. Qi, Z. Lee, C. Hu, and M. Wang, "Requirement of minimal signal-to-noise ratios of ocean color sensors and uncertainties of ocean color products," *J. Geophys. Res. Oceans*, vol. 122, no. 3, pp. 2595–2611, 2017.

[43] R. M. Kudela, S. B. Hooker, H. F. Houskeeper, and M. McPherson, "The Influence of Signal to Noise Ratio of Legacy Airborne and Satellite Sensors for Simulating Next-Generation Coastal and Inland Water Products," *Remote Sens.*, vol. 11, no. 18, 2019.

[44] E. Lancheros, A. Camps, H. Park, P. Sicard, A. Mangin, H. Matevosyan, and I. Lluch, "Gaps Analysis and Requirements Specification for the Evolution of Copernicus System for Polar Regions Monitoring: Addressing the Challenges in the Horizon 2020–2030," *Remote Sens.*, vol. 10, no. 7, 2018.

[45] C. O. Davis, M. Kavanaugh, R. Letelier, W. P. Bissett, and D. Kohler, "Spatial and spectral resolution considerations for imaging coastal waters," in *Coastal Ocean Remote Sensing*, vol. 6680. SPIE, 2007, pp. 196 – 207.

[46] P. Mouroulis and R. O. Green, "Review of high fidelity imaging spectrometer design for remote sensing," *Optical Engineering*, vol. 57, no. 4, 2018.

[47] G. Vane, R. O. Green, T. G. Chrien, H. T. Enmark, E. G. Hansen, and W. M. Porter, "The airborne visible/infrared imaging spectrometer (AVIRIS)," *Remote Sens. Environ.*, vol. 44, no. 2, pp. 127 – 143, 1993.

[48] M. T. Eismann, *Hyperspectral Remote Sensing*, SPIE: Bellingham, WA, 2012.

[49] J. E. Fowler, "Compressive pushbroom and whiskbroom sensing for hyperspectral remote-sensing imaging," in *2014 IEEE Int. Conf. Image Process. (ICIP)*, Oct 2014, pp. 684–688.

[50] D. Jervis, J. McKeever, B. O. A. Durak, J. J. Sloan, D. Gains, D. J. Varon, A. Ramier, M. Strupler, and E. Tarrant, "The GHGSat-D imaging spectrometer," *Atmos. Meas. Tech.*, in review, 2020.

[51] S. Henrot, C. Soussen, and D. Brie, "Fast Positive Deconvolution of Hyperspectral Images," *IEEE Trans. Image Process.*, vol. 22, no. 2, pp. 828–833, 2013.

[52] S. Kay, J. D. Hedley, and S. Lavender, "Sun Glint Correction of High and Low Spatial Resolution Images of Aquatic Scenes: a Review of Methods for Visible and Near-Infrared Wavelengths," *Remote Sens.*, vol. 1, no. 4, pp. 697–730, 2009.

[53] M. Lapadatu, S. Bakken, M. E. Grøtte, M. Alver, and T. A. Johansen, "Simulation Tool for Hyper-Spectral Imaging From a Satellite," in *2019 10th Workshop on Hyperspectral Imaging and Signal Processing: Evolution in Remote Sensing (WHISPERS)*, 2019.

[54] A. Berk, P. Conforti, R. Kennett, T. Perkins, F. Hawes, and J. van den Bosch, "MODTRAN® 6: A major upgrade of the MODTRAN® radiative transfer code," in *2014 6th Workshop on Hyperspectral Image and Signal Processing: Evolution in Remote Sensing (WHISPERS)*, 2014.

[55] J. M. Lerner, "Imaging spectrometer fundamentals for researchers in the biosciences - A tutorial," *Cytometry A*, vol. 69, no. 8, pp. 712–734, 2006.

[56] H. R. Gordon, "Atmospheric correction of ocean color imagery in the Earth Observing System era," *J. Geophys. Res. Atmos.*, vol. 102D, pp. 17 081–17 106, 1997.

[57] M. Wang, "A refinement for the Rayleigh radiance computation with variation of the atmospheric pressure," *Int. J. Remote Sens.*, vol. 26, no. 24, pp. 5651–5663, 2005.

[58] W. J. Moses, J. H. Bowles, R. L. Lucke, and M. R. Corson, "Impact of signal-to-noise ratio in a hyperspectral sensor on the accuracy of biophysical parameter estimation in case II waters," *Opt. Express*, vol. 20, no. 4, pp. 4309–4330, 2012.

[59] T. Skauli, "Sensor noise informed representation of hyperspectral data, with benefits for image storage and processing," *Opt. Express*, vol. 19, no. 14, pp. 13 031–13 046, 2011.

[60] B. A. Franz, S. W. Bailey, P. J. Werdell, and C. R. McClain, "Sensor-independent approach to the vicarious calibration of satellite ocean color radiometry," *Appl. Opt.*, vol. 46, no. 22, pp. 5068–5082, 2007.

[61] B.-C. Gao, R.-R. Li, R. L. Lucke, C. O. Davis, R. M. Bevilacqua, D. R. Korwan, M. J. Montes, J. H. Bowles, and M. R. Corson, "Vicarious calibrations of HICO data acquired from the International Space Station," *Appl. Opt.*, vol. 51, no. 14, pp. 2559–2567, 2012.

[62] B.-C. Gao, M. J. Montes, Z. Ahmad, and C. O. Davis, "Atmospheric correction algorithm for hyperspectral remote sensing of ocean color from space," *Appl. Opt.*, vol. 39, no. 6, pp. 887–896, 2000.

[63] D. K. Clark, M. A. Yarbrough, M. E. Feinholz, S. Flora, Y. S. K. W Broenkow, B. C. Johnson, S. W. Brown, M. Yuen, and J. L. Mueller,

"MOBY, A Radiometric Buoy for Performance Monitoring and Vicarious Calibration of Satellite Ocean Color Sensors: Measurement and Data Analysis Protocols," in *SeaWiFs Postlaunch Technical Report Series*, vol. 2, 2002.

[64] A. Bucholtz, "Rayleigh-scattering calculations for the terrestrial atmosphere," *Appl. Opt.*, vol. 34, no. 15, pp. 2765–2773, 1995.

[65] J. A. Richards and X. Jia, *Remote Sensing Digital Image Analysis: An Introduction*, 3rd ed., D. E. Ricken and W. Gessner, Eds. Berlin, Heidelberg: Springer-Verlag, 1999.

[66] A. M. Sayer, N. C. Hsu, and C. Bettenhausen, "Implications of MODIS bow-tie distortion on aerosol optical depth retrievals, and techniques for mitigation," *Atmos. Meas. Tech.*, vol. 8, no. 12, pp. 5277–5288, 2015.

[67] R. F. Stengel, *Flight Dynamics*. Princeton, NJ: Princeton University Press, 2004.

[68] Y. M. Li, C. j. Li, R. Zheng, X. Li, and J. Yang, "The research on image processing technology of the star tracker," in *International Symposium on Optoelectronic Technology and Application 2014: Image Processing and Pattern Recognition*, vol. 9301. SPIE, 2014, pp. 9–13.

[69] T. S. Rose, D. W. Rowen, S. D. LaLumondiere, N. I. Werner, R. Linares, A. C. Faler, J. M. Wicker, C. M. Coffman, G. A. Maul, D. H. Chien, A. C. Utter, R. P. Welle, and S. W. Janson, "Optical communications downlink from a 1.5U cubesat: OCSD program," in *Proc. Vol. 11180, Int. Conf. Space Opt. - ICSO 2018*, vol. 10910. SPIE, July 2019.

[70] A. Habib, Y. Han, W. Xiong, F. He, Z. Zhang, and M. Crawford, "Automated ortho-rectification of UAV-based hyperspectral data over an agricultural field using frame RGB imagery," *Remote Sens.*, vol. 8, no. 10, 796, 2016.

[71] Consultative Committee for Space Data Systems, *Lossless Multispectral and Hyperspectral Image Compression - CCSDS 123.0-B-1*, Blue Book ed., CCSDS: Reston, VA, 2012, vol. 1.

[72] J. Fjeldtvedt and M. Orlandić, "CubeDMA – Optimizing three-dimensional DMA transfers for hyperspectral imaging applications," *Microprocess. Microsyst.*, vol. 65, pp. 23–36, 2019.

[73] M. Orlandić, J. Fjeldtvedt, and T. A. Johansen, "A Parallel FPGA Implementation of the CCSDS-123 Compression Algorithm," *Remote Sens.*, vol. 11, no. 6, p. 673, 2019.

[74] J. Fjeldtvedt, M. Orlandić, and T. A. Johansen, "An Efficient Real-Time FPGA Implementation of the CCSDS-123 Compression Standard for Hyperspectral Images," *IEEE J. Sel. Topics Appl. Earth Observ. Remote Sens.*, vol. 11, no. 10, pp. 3841–3852, 2018.

[75] S. Bakken, M. Orlandić, and T. A. Johansen, "The effect of dimensionality reduction on signature-based target detection for hyperspectral imaging," in *CubeSats and SmallSats for Remote Sensing III, SPIE Optical Engineering + Applications*, San Diego, USA, 2019.

[76] M. B. Henriksen, J. L. Garrett, E. F. Prentice, A. Stahl, T. A. Johansen, and F. Sigernes, "Real-Time Corrections for a Low-Cost Hyperspectral Instrument," in *2019 10th Workshop on Hyperspectral Imaging and Signal Processing: Evolution in Remote Sensing (WHISPERS)*, 2019.

[77] C. Rodarmel and J. Shan, "Principal Component Analysis for Hyperspectral Image Classification," *Surv. Land Inf. Sci.*, vol. 62, no. 2, pp. 115–122, 2002.

[78] D. Fernández, C. González, D. Mozos, and S. López, "FPGA implementation of the principal component analysis algorithm for dimensionality reduction of hyperspectral images," *J. Real Time Image Process.*, vol. 16, pp. 1–12, 2016.

[79] R. Vitale, A. Zhyrova, J. F. Fortuna, O. E. de Noord, A. Ferrer, and H. Martens, "On-The-Fly processing of continuous high-dimensional data streams," *Chemometr. Intell. Lab Syst.*, vol. 161, pp. 118–129, 2017.

[80] H. Martens, J. P. Nielsen, and S. B. Engelsen, "Light Scattering and Light Absorbance Separated by Extended Multiplicative Signal Correction. Application to Near-Infrared Transmission Analysis of Powder Mixtures," *Analytical Chemistry*, vol. 75, no. 3, pp. 394–404, 2003.

[81] D. Manolakis and G. Shaw, "Detection algorithms for hyperspectral imaging applications," *IEEE Signal Process. Mag.*, vol. 19, no. 1, pp. 29–43, 2002.

[82] D. G. Manolakis, "Taxonomy of detection algorithms for hyperspectral imaging applications," *Opt. Eng.*, vol. 44, no. 6, pp. 066 403–1–11, 2005.

[83] D. Boskovic, M. Orlandić, and T. A. Johansen, "A reconfigurable multimode implementation of hyperspectral target detection algorithms," *Microprocess. Microsyst.*, vol. 78, 2020.

[84] D. Boskovic, M. Orlandić, S. Bakken, and T. A. Johansen, "HW/SW Implementation of Hyperspectral Target Detection Algorithm," in *8th Mediterranean Conf. on Embedded Computing – MECO*, 2019.

[85] A. Alcolea, M. E. Paoletti, J. M. Haut, J. Resano, and A. Plaza, "Inference in Supervised Spectral Classifiers for On-Board Hyperspectral Imaging: An Overview," *Remote Sens.*, vol. 12, no. 3, 534, 2020.

[86] Y. Zhao, Y. Yuan, and Q. Wang, "Fast Spectral Clustering for Unsupervised Hyperspectral Image Classification," *Remote Sens.*, vol. 11, no. 399, 2019.

[87] R. Wang, F. Nie, and W. Yu, "Fast Spectral Clustering With Anchor Graph for Large Hyperspectral Images," *IEEE Geosci. Remote Sens. Lett.*, vol. 14, no. 11, pp. 2003–2007, 2017.

[88] M. Ismail and M. Orlandić, "Segment-Based Clustering of Hyperspectral Images Using Tree-Based Data Partitioning Structures," *Algorithms*, vol. 13, no. 12, 330, 2020.

[89] T. Opsahl, T. V. Haavardsholm, and I. Winjum, "Real-time georeferencing for an airborne hyperspectral imaging system," in *Algorithms and Technologies for Multispectral, Hyperspectral, and Ultraspectral Imagery XVII*, vol. 8048. SPIE, 2011, pp. 290–295.

[90] D. Schläpfer and R. Richter, "Geo-atmospheric processing of airborne imaging spectrometry data. Part 1: Parametric orthorectification," *Int. J. Remote Sens.*, vol. 23, no. 13, pp. 2609–2630, 2002.

[91] S. C. Park, M. K, Park, and M. G. Kang, "Super-resolution image reconstruction: a technical overview," *IEEE Signal Process. Mag.*, vol. 20, no. 3, pp. 21–36, 2003.

[92] J. L. Garrett, D. Langer, K. Avagian, and A. Stahl, "Accuracy of super-resolution for hyperspectral ocean observations," in *OCEANS 2019 - Marseille*, 2019.

[93] L. Clarisse, M. Van Damme, C. Clerbaux, and P.-F. Coheur, "Tracking down global NH_3 point sources with wind-adjusted superresolution," *Atmos. Meas. Tech.*, vol. 12, pp. 5457–5473, 2019.

[94] H. Stark and P. Oskoui, "High-resolution image recovery from image-plane arrays, using convex projections," *J. Opt. Soc. Am. A*, vol. 6, no. 11, pp. 1715–1726, 1989.

[95] S. Farsiu, M. Robinson, M. Elad, and P. Milanfar, "Fast and Robust Multiframe Super Resolution," *IEEE Trans. Image Process.*, vol. 13, no. 10, pp. 1327–1344, 2004.

[96] S. Baker and T. Kanade, "Limits on super-resolution and how to break them," *IEEE Trans. Pattern Anal. Mach. Intell.*, vol. 24, no. 9, pp. 1167–1183, 2002.

[97] T. Köhler, M. Bätz, F. Naderi, A. Kaup, A. Maier, and C. Riess, "Toward Bridging the Simulated-to-Real Gap: Benchmarking Super-Resolution on Real Data," *IEEE Trans. Pattern Anal. Mach. Intell.*, vol. 42, no. 11, pp. 2944–2959, 2019.

[98] J. Yang, J. Wright, T. S. Huang, and Y. Ma, "Image Super-Resolution Via Sparse Representation," *IEEE Trans. Image Process.*, vol. 19, no. 11, pp. 2861–2873, 2010.

[99] J. Kim, J. Kwon Lee, and K. Mu Lee, "Accurate Image Super-Resolution Using Very Deep Convolutional Networks," in *Proc. IEEE Comput. Soc. Conf. Comput. Vis. Pattern Recognit.*, 2016, pp. 1646–1654.

[100] S. Anwar, S. Khan, and N. Barnes, "A Deep Journey into Super-Resolution: A Survey," *ACM Computing Surveys*, vol. 53, no. 3, 2020.

[101] C. Lanaras, E. Baltsavias, and K. Schindler, "Hyperspectral Super-Resolution by Coupled Spectral Unmixing," in *Proc. IEEE Int. Conf. Comput. Vis. (ICCV)*, 2015, pp. 3586–3594.

[102] N. Yokoya, C. Grohnfeldt, and J. Chanussot, "Hyperspectral and Multispectral Data Fusion: A comparative review of the recent literature," *IEEE Geosci. Remote Sens. Mag.*, vol. 5, no. 2, pp. 29–56, 2017.

[103] T. Akgun, Y. Altunbasak, and R. M. Mersereau, "Super-resolution reconstruction of hyperspectral images," *IEEE Trans. Image Process.*, vol. 14, no. 11, pp. 1860–1875, 2005.

[104] K. Avagian and M. Orlandić, "An Efficient FPGA Implementation of Richardson-Lucy Deconvolution Algorithm for Hyperspectral Images," *Electronics*, vol. 10, no. 4, 504, 2021.

[105] K. Avagian, M. Orlandić, and T. A. Johansen, "An FPGA-oriented HW/SW Codesign of Lucy-Richardson Deconvolution Algorithm for Hyperspectral Images," in *8th Mediterranean Conf. on Embedded Computing (MECO)*, 2019.

[106] R. S. Fraser, S. Mattoo, E.-N. Yeh, and C. R. McClain, "Algorithm for atmospheric and glint corrections of satellite measurements of ocean pigment," *J. Geophys. Res. Atmos.*, vol. 102, pp. 17 107–17 118, 1997.

[107] T. Schroeder, I. Behnert, M. Schaale, J. Fischer, and R. Doerffer, "Atmospheric correction algorithm for MERIS above case-2 waters," *Int. J. Remote Sens.*, vol. 28, no. 7, pp. 1469–1486, 2007.

[108] IOCCG, *Atmospheric Correction for Remotely-Sensed Ocean-Colour Products*, M. Wang, Ed., Reports of the International Ocean-Colour Coordinating Group, No. 10, IOCCG: Dartmouth, NS, Canada, 2010.
[109] B. Gao and R. Li, "Spectral calibrations of HICO data using atmospheric bands and radiance adjustment based on HICO and MODIS data comparisons," in *2010 IEEE Int. Geosci. Remote Sens. Symp.*, 2010, pp. 4260–4263.
[110] K. Stamnes, B. Hamre, S. Stamnes, N. Chen, Y. Fan, W. Li, Z. Lin, and J. Stamnes, "Progress in Forward-Inverse Modeling Based on Radiative Transfer Tools for Coupled Atmosphere-Snow/Ice-Ocean Systems: A Review and Description of the AccuRT Model," *Appl. Sci.*, vol. 8, no. 12, 2682, 2018.
[111] O. M. Borge, S. Bakken, and T. A. Johansen, "Atmospheric correction of hyperspectral data over coastal waters based on machine learning models," in *11th Workshop on Hyperspectral Imaging and Signal Processing: Evolution in Remote Sensing (WHISPERS)*, in review, 2021.

Mariusz E. Grøtte received his M.Sc. degree in Aerospace Engineering from Georgia Institute of Technology in 2015 and B.Eng. (Honours) degree in Aerospace Engineering from the University of Manchester in 2013. He is currently a Ph.D. candidate in the Department of Engineering Cybernetics, NTNU, and was Visiting Researcher at NASA Ames Research Center from 2018 to 2019. His research focuses on multi-agent coordinated robotic and small-satellite remote sensing, nonlinear control and optimal control.

Roger Birkeland received his M.Sc. in Electronic Engineering at NTNU and is a post-doctoral researcher at NTNU in the Department of Electronic Systems. He received his Ph.D. in satellite communications in 2019 and is currently researching small satellite systems and heterogeneous communication systems for remote areas.

Evelyn Honoré-Livermore received her M.Sc. in Electronic Engineering at NTNU and her MBA from Yonsei University in Seoul. She is a Ph.D. fellow in the Department of Electronic Systems, NTNU. She is researching systems engineering and project management methods for academic research projects. She is also the project manager of the HYPSO project.

Sivert Bakken is a Ph.D. candidate at Department of Engineering Cybernetics, NTNU. Researching how to utilize small satellites with hyperspectral imager as an intelligent agent in coordinated missions involving autonomous agents, developing methods to advance the usefulness of ocean color data. he is responsible for the software development on the satellite(s).

Joseph L. Garrett received a BSc in Physics and Mathematics from the Ohio State University in 2011 and a Ph.D. in Physics from the University of Maryland in 2017. He now studies hyperspectral imaging and image processing from satellites and drones as a postdoctoral researcher at NTNU.

Elizabeth F. Prentice is a Ph.D. fellow in the Department of Engineering Cybernetics at NTNU. She is researching optical remote sensing and mechanical integration for small satellites and robotic agents. She is responsible for hardware development on the HYPSO mission at NTNU.

Fred Sigernes is a full Professor in optics and atmospheric research at the University Centre in Svalbard (UNIS), and he is head of the Kjell Henriksen Observatory (KHO) at Breinosa. He is a team leader for the ground-based activity at the Birkeland Centre for Space Science (BCSS) at University of Bergen and Professor II at AMOS, NTNU. His main expertise is spectroscopy with focus on aurora.

Milica Orlandić received a B.Sc. and M.Sc. degrees in electrical engineering from the University of Montenegro in 2007 and 2009. She received a Ph.D. degree in electronics from NTNU in 2015. She currently holds the position of Associate Professor in Electronic Systems Engineering at NTNU. Her research interests include digital hardware design of hyperspectral imaging, satellite onboard processing systems, and high-performance reconfigurable systems.

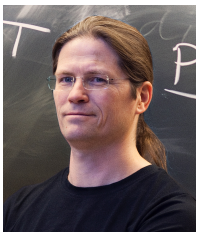

J. Tommy Gravdahl received the Siv.ing and Dr.Ing degrees in engineering cybernetics from the Norwegian University of Science and Technology (NTNU), Trondheim, Norway, in 1994 and 1998, respectively. He was appointed Associate Professor and Professor with the Department of Engineering Cybernetics, NTNU, in 2001 and 2005, respectively. He was the Head of the Department of Engineering Cybernetics from 2008 to 2009. He has supervised the graduation of 140 M.Sc. and 14 Ph.D. candidates. He has published five books and more than 250 articles in international conferences and journals. His current research interests include mathematical modeling and nonlinear control in general, in particular applied to turbomachinery, marine vehicles, spacecraft, robots, and high-precision mechatronic systems. Dr. Gravdahl is currently a Senior Editor of the Mechatronics (IFAC journal) and an Associate Editor of the IEEE Transactions on Control Systems Technology. He received the IEEE Transactions on Control Systems Technology Outstanding Paper Award in 2000 and 2017.

Tor A. Johansen received the MSc degree in 1989 and the PhD degree in 1994, both in electrical and computer engineering, from the NTNU, Trondheim, Norway. From 1995 to 1997, he worked at SINTEF as a researcher before he was appointed Associated Professor at the NTNU in Trondheim in 1997 and Professor in 2001. He has published several hundred articles in the areas of control, estimation and optimization with applications in the marine, aerospace, automotive, biomedical and process industries. In 2002 Johansen co-founded the company Marine Cybernetics AS where he was Vice President until 2008. Prof. Johansen received the 2006 Arch T. Colwell Merit Award of the SAE, and is currently a principal researcher within the Center of Excellence on Autonomous Marine Operations and Systems (NTNU-AMOS) and director of the Unmanned Aerial Vehicle Laboratory at NTNU and the SmallSat Laboratory at NTNU. He recently co-founded the spin-off companies Scout Drone Inspection, UBIQ Aerospace, Zeabuz and SentiSystems.